Article:
Abuarab, N, Munsey, TS, Jiang, L-H orcid.org/0000-0001-6398-0411 et al. (2 more authors) (2017) High glucose–induced ROS activates TRPM2 to trigger lysosomal membrane permeabilization and Zn2+-mediated mitochondrial fission. Science Signaling, 10 (490). eaal4161. ISSN 1945-0877

https://doi.org/10.1126/scisignal.aal4161

One-sentence summary: ROS produced in response to high glucose trigger mitochondrial fragmentation through a TRPM2-mediated pathway.

Editor's summary:
Fragmented by diabetic stress
The high circulating glucose concentrations characteristic of diabetes induce the excessive production of reactive oxygen species (ROS), which triggers mitochondrial fragmentation. The cation channel TRPM2 is activated by ROS, leading Abuarab *et al.* to investigate the role of this channel in mitochondrial fragmentation in endothelial cells, which become dysfunctional in diabetics. In response to high glucose–induced oxidative stress, Ca^{2+} influx through TRPM2 channels caused lysosomal permeabilization and redistribution of lysosomal Zn^{2+} to mitochondria. The increase in mitochondrial Zn^{2+} led to the recruitment of the fission factor Drp-1, resulting in mitochondrial fragmentation. This pathway may play a role in the pathology of aging-associated diseases that are characterized by increased mitochondrial fragmentation.

High glucose-induced ROS activates TRPM2 to trigger lysosomal membrane permeabilization and Zn^{2+}-mediated mitochondrial fission

Nada Abuarab[1,2,4], Tim S. Munsey[1], Lin-Hua Jiang[1], Jing Li[2,3] and Asipu Sivaprasadarao[1,2,*]

[1]School of Biomedical Sciences, Faculty of Biological Sciences, [2]Multidisciplinary Cardiovascular Research Centre, [3]School of Medicine, University of Leeds, LS2 9JT, Leeds, U.K. [4]College of Science and Health Professions, King Saud bin Abdulaziz University for Health Sciences, P.O.Box 9515, Jeddah 21423, Saudi Arabia.

Corresposnding author:
Professor Asipu Sivaprasadarao
School of Biomedical Sciences
G6.44d, Garstang Building
University of Leeds
Leeds
LS2 9JT UK
Tel: +44-(0)-113-3434326
Fax: +44-(0)-113-3431407
E-mail: a.sivaprasadarao@leeds.ac.uk

ABSTRACT

Diabetic stress increases the production of reactive oxygen species (ROS), leading to mitochondrial fragmentation and dysfunction. We hypothesized that ROS-sensitive TRPM2 channels mediated diabetic stress-induced mitochondrial fragmentation. We found that chemical inhibitors, RNAi silencing and genetic knock-out of TRPM2 channels abolished the ability of high glucose to cause mitochondrial fission in endothelial cells, a cell type that is particularly vulnerable to diabetic stress. Similar to high glucose, increasing ROS in endothelial cells by applying H_2O_2 induced mitochondrial fission. Ca^{2+} that entered through TRPM2 induced lysosomal membrane permeabilization, which led to the release of lysosomal Zn^{2+} and a subsequent increase in mitochondrial Zn^{2+}. Zn^{2+} promoted the recruitment of the fission factor Drp-1 to mitochondria to trigger their fission. This signaling pathway may operate in aging-associated illnesses in which excessive mitochondrial fragmentation plays a central role.

INTRODUCTION

About 10% of the global population currently suffers from diabetes. Diabetes is a major risk factor for many late-onset diseases that include cardiovascular diseases, neuronal diseases and cancer (*1-3*). In diabetic patients, tissues are exposed to abnormally high blood amounts of glucose, fats and pro-inflammatory cytokines (collectively known as 'diabetic milieu') (*1, 4, 5*). Tissues exposed to diabetic milieu experience oxidative stress due to increased production of reactive oxygen species (ROS) (*4-6*). ROS target various mechanisms that contribute to diabetes-associated diseases, among which mitochondrial dynamics is emerging as an important disease mechanism (*7, 8*). By triggering abnormal mitochondrial fragmentation, ROS impair mitochondrial function, thereby contributing to disease states (*8-12*). That mitochondrial dynamics contributes to the disease state is highlighted by the rescue of oxidative stress-induced dysfunction of many cell types by inhibition of mitochondrial fragmentation (*13-15*). Thus mitochondrial dynamics represents an attractive therapeutic target for many late-onset diseases (*8, 9, 16, 17*). To fully realise this potential, however, requires a better understanding of the molecular and cellular mechanisms responsible for abnormal mitochondrial fragmentation.

Eukaryotic cells maintain a healthy mitochondrial network by regulating the balance between mitochondrial fusion and fission processes, collectively known as mitochondrial dynamics (*7-10, 18*). Oxidative stress, including that imposed by the diabetic milieu, tips this balance towards mitochondrial fission, leading to fragmented, dysfunctional mitochondria in the cell (*7-9, 11-13, 18, 19*). Mitochondrial fusion is mediated by three GTPases: Mfn1, Mfn2 and Opa1 (*8-10, 16, 18*). Fission is mediated by the dynamin-related protein (Drp)-1, another GTPase that forms oligomeric spirals to constrict mitochondria at sites where specific adaptors (Mff, Mid49-51 and Fis1) are located (*9, 16*). Under normal conditions, Drp-1 is mainly localised to the cytoplasm, but during oxidative stress, it is recruited to the network at sites marked and pre-constricted by the ER tubules (*20*). Drp-1 recruitment to mitochondria is regulated and Ca^{2+} dependent (*21, 22*).

In this study, we hypothesised that ROS-sensitive TRPM2 ion channels mediated oxidative stress-induced mitochondrial fission because oxidative stress stimulates TRPM2 channels, and activation of TRPM2 increases intracellular cytosolic Ca^{2+} concentrations (*23-25*) required for mitochondrial fission (*21, 22*). To address our hypothesis, we selected endothelial cells, because these cells are harmed by the diabetic milieu. When exposed to high glucose, they display extensive mitochondrial fragmentation and do not respond to agonist-stimulated activation of nitric oxide synthase and cGMP production, an effect that is rescued by inhibition of fragmentation through silencing of Fis1 and Drp-1 (*12*). Furthermore,

TRPM2 channels are present in endothelial cells (*26*). Our results demonstrate a role for TRPM2 channels in oxidative stress-induced mitochondrial fragmentation, and reveal a signalling cascade that links oxidative stress to mitochondrial fission.

RESULTS

TRPM2 channels mediate oxidative stress-induced mitochondrial fragmentation

To test our hypothesis, we transfected HUVECs (human umbilical vein endothelial cells) with pmito-Cherry, a plasmid construct that allows labelling of mitochondria with the cherry fluorescent reporter protein. Consistent with previous reports, high glucose (33 mM) caused extensive breakdown of the mitochondrial network, resulting in small, rounded structures (Fig. 1A). By contrast, cells exposed to normal glucose concentration (5.6 mM), or normal glucose plus mannitol (to exclude potential osmotic effects by the excess glucose), displayed a healthy mitochondrial network comprising long, branched tubular networks. High glucose caused a significant reduction in both the aspect ratio (length to width ratio) and the form factor (a measure of degree of branching) of mitochondria (Fig. 1, B to D). Inhibition of TRPM2 channels with the nonspecific channel inhibitor 2-aminoethoxydiphenyl borate (2-APB) (*27*) or TRPM2 silencing RNA (fig. S1, A and B), prevented mitochondrial fragmentation (Fig. 1 A to E). By contrast, siRNA-mediated silencing of Stim-1 and Orai-1, which play a major role in store-operated Ca^{2+} entry in endothelial cells, or their selective inhibition with Synta66 (*28*), failed to prevent high glucose-induced mitochondrial fragmentation (fig. S2, A and B). These data indicate that TRPM2 channels play a key role in high glucose-induced mitochondrial fragmentation.

High glucose is not a direct activator of TRPM2 channels, but, as reported previously (*12, 29*), high glucose increased ROS production within cells (Fig. 1F). The high glucose-induced increase in ROS thus appeared to be sufficient to activate TRPM2 channels and thereby cause mitochondrial fragmentation. Consistent with this argument, quenching of ROS with N-acetyl cysteine prevented high glucose-induced mitochondrial fragmentation (Fig. 1G and H). Acute activation of TRPM2 channels with H_2O_2 caused mitochondrial fragmentation in a manner that was blocked by 2-APB or TRPM2 siRNA (fig. S1, C to E), supporting a role for these channels in mitochondrial dynamics.

To seek further evidence for the role of TRPM2 channels in mitochondrial dynamics, we also used HEK-293 cells which lack TRPM2 channels (*30, 31*). H_2O_2 did not affect mitochondrial morphology in these cells, but heterologous expression of TRPM2 channels led to extensive fragmentation (fig. S1F). In an alternative approach, we compared the effect of high glucose

on the mitochondrial network of primary endothelial cells from wild-type mice with those from TRPM2 knock-out (TRPM2-KO) mice. We confirmed the identity of isolated endothelial cells by immunostaining for the endothelial marker CD-31 (also known as PECAM-1). Similar to HUVECs, MitoTracker Red staining showed that high glucose caused extensive mitochondrial fragmentation in primary endothelial cells from wild-type mice (Fig. 2, A to C). Endothelial cells isolated from TRPM2-KO mice, however, were remarkably resistant to high glucose-induced mitochondrial fragmentation (Fig. 2, D to F). Finally, mitochondria in the endothelial cells of intact aorta from TRPM2-KO mice did not undergo fragmentation in response to high glucose (fig. S3). Together, we provided several lines of evidence (pharmacological, siRNA, knock-out and HEK cell data) to support our hypothesis that TRPM2 channels play a key role in oxidative stress-induced mitochondrial fragmentation.

TRPM2 channels regulate mitochondrial fragmentation through Ca^{2+}-induced changes in Zn^{2+} dynamics

Ca^{2+} is required for mitochondrial fragmentation (*21, 22*). However, TRPM2 channels not only conduct Ca^{2+}, but also regulate intracellular Zn^{2+} dynamics (*23, 24, 31, 32*). To exclude a role for Zn^{2+}, we used DTPA (diethylenetriaminepentaacetic acid) and TPEN (N,N,N',N'-tetrakis(2-pyridinylmethyl)-1,2-ethanediamine) (*31*). Chelation of extracellular Zn^{2+} with DTPA failed to prevent H_2O_2-induced mitochondrial fission (fig. S8), suggesting that extracellular Zn^{2+} entry did not contribute to mitochondrial fission. By contrast, TPEN, which unlike DTPA also chelates intracellular Zn^{2+}, abolished the ability of high glucose and H_2O_2 to induce mitochondrial fragmentation (Fig. 3, A to D; fig. S4, A to D), suggesting that Zn^{2+} was likely released from an intracellular site. The effect of TPEN was not due to Ca^{2+} chelation, because the concentation used here is too low (0.3 μM) to bind Ca^{2+} (*30, 31, 33*) . Furthermore, the Zn^{2+} chelating agent clioquinol (*31*) also prevented H_2O_2-induced mitochondrial fission (fig. S4, A to D). In addition, raising the cytosolic concentrations of Zn^{2+} with the Zn^{2+}-specific ionophore pyrithione (Zn-PTO) (*30*) caused extensive mitochondrial fragmentation, and this effect was rescued by TPEN (Fig. 3, E and F). Together, these data revealed a role for Zn^{2+} in oxidative stress-induced mitochondrial dynamics, prompting further investigation into the relative roles of Ca^{2+} and Zn^{2+}.

We were unable to directly test the role of Ca^{2+} in mitochondrial fragmentation, because the currently available Ca^{2+} chelators, including BAPTA-AM, binds Zn^{2+} more avidly than Ca^{2+} (*33*) and thus are not selective for Ca^{2+} (*30*). As an alternative approach, we increased the cytosolic concentrations of Ca^{2+} using the Ca^{2+} ionophore A23187 (Fig. 3, G to I). Consistent with previous reports (*34, 35*), A23187 induced significant mitochondrial fragmentation (Fig. 3, J and K). However, unlike Zn-PTO, A23187 required longer incubation times to cause mitochondrial fragmentation. We have previously demonstrated that TRPM2-mediated Ca^{2+}

entry stimulates intracellular Zn^{2+} release (*31*). We therefore asked whether A23187-induced mitochondrial fission could be mediated by Ca^{2+}-induced changes in intracellular Zn^{2+} dynamics. Consistent with this possibility, TPEN significantly reduced A23187-induced mitochondrial fission (Fig. 3, J and K). Finally, RNAi silencing of TRPM2 did not prevent mitochondrial fragmentation induced by A23187 (fig. S5, A and B) and Zn-PTO (fig. S5, A and C) indicating that TRPM2 channels did not contribute to ionophore-induced effects on mitochondria. Together, these data indicate that TRPM2-mediated Ca^{2+} entry affects intracellular Zn^{2+} dynamics, and thereby mitochondrial fragmentation.

TRPM2 activation and Ca^{2+} entry cause lysosomal membrane permeabilisation

To understand how oxidative stress affects the Zn^{2+} dynamics, we first examined the intracellular distribution of free Zn^{2+}. Co-staining for Zn^{2+} and organelle markers revealed that, as with other cell types (*31, 36*), free Zn^{2+} largely localised to lysosomes in HUVECs as was apparent from the overlap (yellow) of Zn^{2+} staining (FluoZin-3, green) with lysosomal staining (LysoTracker Red) (fig. S6A). Exposure to high glucose (but not to mannitol) caused a decrease in the number of vesicles containing free Zn^{2+}, which was accompanied by a parallel decrease in the number of LysoTracker Red-positive vesicles (Fig. 4, A and B). Similar results were obtained when oxidative stress was directly imposed with H_2O_2 (fig. S6, B and C). The decrease in the number of LysoTracker Red positive vesicles was not an artefact resulting from reduced uptake of the LysoTracker Red dye because H_2O_2 caused release of cathepsin B from lysosomes (fig. S7, A and B). These results suggest that high glucose and H_2O_2, like other oxidative insults (*37*), induce lysosomal membrane permeabilisation and that lysosomal membrane permeabilisation causes loss of lysosomal Zn^{2+}.

Our data suggested that TRPM2-mediated Ca^{2+} entry affects intracellular Zn^{2+} dynamics (Fig. 4, A; fig. S6, B). Because lysosomal membrane permeabilisation mobilised lysosomal Zn^{2+}, we examined the role of TRPM2 channels and Ca^{2+} entry on lysosomal membrane permeabilisation. TRPM2-siRNA, but not scrambled siRNA, inhibited lysosomal membrane permeabilisation induced by both high glucose (Fig. 4, A and B) and H_2O_2 (fig. S6, B and C) and the associated loss of lysosomal Zn^{2+}. To confirm the role of TRPM2 in lysosomal membrane permeabilisation, we used HEK-293-TRPM2^{tet} cells, which express TRPM2 channels only when induced with tetracycline. In the absence of tetracycline, H_2O_2 did not affect the number of lysosomes, but when TRPM2 expression was induced with tetracycline, cells displayed robust lysosomal membrane permeabilisation (Fig. 4, C and D). Together, these results provide evidence that lysosomal membrane permeabilisation is not a nonspecific process, but is regulated by a Ca^{2+} channel. To demonstrate that Ca^{2+} entry drives lysosomal membrane permeabilisation, we increased the cytosolic concentrations of

Ca^{2+} with A23187, which triggered lysosomal membrane permeabilisation (Fig. 4, E and F). siRNA-mediated silencing of TRPM2 chanels failed to prevent A23187-induced lysosomal permeabilisation, indicating that TRPM2 acts upstream in the signalling cascade (Fig. 4G). Together, our data demonstrate that oxidative stress causes lysosomal membrane permeabilisation by stimulating TRPM2-mediated extracellular Ca^{2+} entry. Although the precise mechanisms by which Ca^{2+} entry induces lysosomal membrane permeabilisation remain to be investigated, these results demonstrate that Ca^{2+}-induced lysosomal membrane permeabilisation leads to the mobilisation of lysosomal Zn^{2+}.

TRPM2-induced lysosomal membrane permeabilisation is accompanied by an increase in mitochondrial Zn^{2+}

Although lysosomal membrane permeabilisation caused release of lysosomal Zn^{2+}, there was no detectable increase in cytosolic Zn^{2+} (Fig. 4, A; fig. S6, B). Because mitochondria can sequester free Zn^{2+} (*31, 38*), and because mitochondrial fission was prevented by Zn^{2+} chelation (Fig. 3, A to F, J and K), we asked whether Zn^{2+} released during lysosomal membrane permeabilisation was removed by mitochondria. To test this notion, we co-stained high glucose-treated cells with FluoZin-3 and MitoTracker Red to label Zn^{2+} (green) and mitochondria (red) respectively. The numerous yellow puncta in merged images of high glucose-treated cells indicated the presence of Zn^{2+} in fragmented mitochondria. By contrast, in control and mannitol-treated cells, the mitochondrial network was intact and there was no detectable free Zn^{2+} in mitochondria (Fig. 5, A to C). We also examined high glucose- and H_2O_2-induced increases in mitochondrial Zn^{2+} using cells expressing modest amounts of Mito-Cherry. We selected cells showing partial fragmentation to visualise mitochondria on their way to full fragmentation using instant Structured Illumination Microscopy (iSIM) (*39*). The resulting high resolution images showed the presence of Zn^{2+} in partially broken mitochondria (Fig. 5, D). These data suggest that an increase in mitochondrial Zn^{2+} likely triggered mitochondrial fragmentation. To confirm that lysosomal membrane permeabilisation contributed to the increase in mitochondrial Zn^{2+}, we blocked the lysosomal membrane permeabilisation-mediated lysosomal Zn^{2+} release with TRPM2 siRNA, which attenuated high glucose-induced mitochondrial Zn^{2+} accumulation and as expected, was accompanied by inhibition of mitochondrial fragmentation (Fig. 5, A to C). Similar results were obtained in H_2O_2-treated cells (fig. S9, A and B). Together, these data indicate that Zn^{2+} released during lysosomal membrane permeabilisation is redistributed to mitochondria.

TRPM2 dependent increase in mitochondrial Zn^{2+} promotes Drp-1 recruitment

Mitochondrial fragmentation is initiated by the recruitment of Drp-1, a GTPase that catalyses mitochondrial fragmentation (*8, 9, 16, 18, 22, 40*). We postulated that the TRPM2-dependent

increase in mitochondrial Zn^{2+} induced Drp-1 recruitment. To test this notion, we transfected HUVECs with Drp-1-GFP (a construct that suppresses the activity of endogenous Drp1) (*22*) and monitored its recruitment from the cytoplasm to mitochondria. High glucose, but not mannitol, promoted Drp-1 mitochondrial recruitment, as assessed by the co-localisation of fluorescence of MitoTracker Red with that of Drp-1-GFP (Fig. 6, A and B). TRPM2-siRNA suppressed recruitment of Drp-1-GFP, but not the dominant negative Drp-1-GFP, in response to high glucose (Fig. 6, A and B). Furthermore, RNAi silencing of Drp-1, as well as its partners, Fis-1 and MFF, prevented high glucose-induced mitochondrial fragmentation (Fig. 6, C and D). Together, these results suggested that TRPM2 activation leads to Drp-1 recruitment and mitochondrial fragmentation.

We next asked whether Zn^{2+} contributes to Drp-1 recruitment. Chelation of Zn^{2+} with TPEN markedly inhibited high glucose-induced Drp-1-GFP recruitment (Fig. 6, A and B). Furthermore, delivery of Zn^{2+} through Zn-PTO stimulated mitochondrial recruitment of Drp-1-GFP, but not its dominant negative version (Fig. 6, E and F). Together, we conclude that TRPM2-mediated increase in mitochondrial Zn^{2+} promotes Drp-1 recruitment and subsequent mitochondrial fragmentation.

DISCUSSION

Hyperglycaemia is a major risk factor for various human diseases. Multiple studies have reported that mitochondrial dynamics play a key role in the pathophysiology of diabetes and diabetes-associated complications (*7, 8*). Cell-based studies have shown that hyperglycaemic conditions cause abnormal mitochondrial fragmentation by increasing the production of ROS (*11, 12, 29*). However, the underlying signalling mechanisms are not fully understood. Using endothelial cells as a model system (*12*), we report a signalling pathway that linked high glucose-induced ROS production to mitochondrial fragmentation (fig. S10). The pathway entailed extracellular Ca^{2+} entry through ROS-activated TRPM2 channels, Ca^{2+}-induced lysosomal membrane permeabilisation, redistribution of lysosomal Zn^{2+} to mitochondria, and Zn^{2+}-induced mitochondrial recruitment of Drp-1 and mitochondrial fragmentation.

Using pharmacological, RNA-interference and gene knock-out approaches, we demonstrated that ROS-sensitive TRPM2 channels mediate oxidative stress (high glucose and H_2O_2)-induced mitochondrial fragmentation (Fig. 1, A to E, Fig. 2, A to G, fig. S1, C to F and fig. S3). To gain insight into the underlying mechanism, we examined the roles of Ca^{2+} and Zn^{2+} because the intracellular concentrations of both of these ions are increased by TRPM2 activation (*23, 24, 30-32*). Although Ca^{2+} is implicated in mitochondrial fragmentation (*21, 22, 41, 42*), our results demonstrated that chelation of Zn^{2+} alone was sufficient to

prevent mitochondrial fragmentation (Fig. 3, A to D and fig. S4, A-D). This role for Zn^{2+} was further supported by the finding that delivery of Zn^{2+} through the zinc ionophore, Zn-PTO, caused mitochondrial fragmentation (Fig. 3, E and F). The lack of Ca^{2+}-specific chelators (*30, 33*) prevented us from directly testing the role of TRPM2-mediated Ca^{2+} entry in mitochondrial fission. We have therefore used the Ca^{2+}-ionophore, A23187, which raises cytosolic concentrations of Ca^{2+}, but not Zn^{2+} (*30*). Consistent with the previous reports (*34, 35*), A23187 caused mitochondrial fission, but required longer incubation times (>2 hrs) to elicit this effect (Fig. 3, J and K), which was inhibited by the Zn^{2+} chelator TPEN (Fig. 3, J and K). These results imply that Zn^{2+} plays a crucial role in Ca^{2+}-induced mitochondrial fission.

Although TRPM2 channels can promote Zn^{2+} entry (*31, 32*), chelation of extracellular Zn^{2+} with the membrane impermeable DTPA reagent failed to prevent mitochondrial fragmentation (fig. S8), suggesting that the free Zn^{2+} required for mitochondrial fragmentation must come from an intracellular site. The majority of intracellular Zn^{2+} is protein bound (*33*) except in lysosomes where the acidic pH allows Zn^{2+} to exist in its free state (*31, 36*). We asked whether lysosomal Zn^{2+} was mobilised to affect mitochondrial dynamics. We found that both high glucose and H_2O_2 trigger lysosomal membrane permeabilisation, resulting in the loss of lysosomal Zn^{2+} (Fig. 4, A and B; fig. S6, B and C). These results were not surprising because oxidative stress causes lysosomal membrane permeabilisation (*37, 43, 44*) and because both high glucose and H_2O_2 are stress inducing substances. Unexpectedly, however, we found that pharmacological inhibition or knockdown of TRPM2 channels prevented high glucose- and H_2O_2 -induced lysosomal membrane permeabilisation and the consequent loss of lysosomal Zn^{2+} (Fig. 4, A and B, fig. S6, B and C). These findings demonstrate that lysosomal membrane permeabilisation is not a nonspecific process (*37*), but is regulated by an ion channel. Because the TRPM2 channel is primarily a Ca^{2+} channel, we suspected that extracellular Ca^{2+} entry could stimulate lysosomal membrane permeabilisation by activating lipases such as phospholipase A2, sphingomyelinase and phospholipase C (*43, 45*). Indeed, increased cytosolic Ca^{2+} with A23187 caused a marked increase in lysosomal membrane permeabilisation (Fig. 4, E and F). Together, our results indicate that TRPM2-mediated Ca^{2+} entry stimulates lysosomal membrane permeabilisation. These findings are important from a pathophysiological perspective because lysosomal membrane permeabilisation is linked to various human diseases, including vascular diseases (*44*).

Although lysosomal membrane permeabilisation led to the loss of lysosomal Zn^{2+}, we found an increase in mitochondrial Zn^{2+}, rather than in cytoplasmic Zn^{2+}. Inhibition of lysosomal membrane permeabilisation with TRPM2-siRNA attenuated both high glucose- and H_2O_2-

induced increase in mitochondrial Zn^{2+} (Fig. 5, A and B; fig. S9, A and B) indicating mobilisation of lysosomal Zn^{2+} to mitochondria. Although how this transfer occurs remains to be investigated, mitochondria have several transport mechanisms, such as the mitochondrial Ca^{2+} uniporter (*38*), to facilitate Zn^{2+} uptake. Regardless of how Zn^{2+} enters mitochondria, we did not see mitochondrial fragmentation in the absence of an increase in mitochondrial Zn^{2+}. Thus, our results indicate that, by raising the mitochondrial Zn^{2+}, TRPM2-mediated lysosomal membrane permeabilisation causes mitochondrial fission.

A critical step in mitochondrial fission is the recruitment of Drp-1 from the cytoplasm to mitochondria (*8, 9, 16*). Accordingly, high glucose increased the recruitment of heterologously expressed Drp-1-GFP to mitochondria (Fig. 6, A and B). Moreover, inhibition of TRPM2 channels and hence of lysosomal membrane permeabilisation or chelation of Zn^{2+} prevented Drp-1-GFP recruitment (Fig. 6, A and B), suggesting that mobilisation of lysosomal Zn^{2+} to mitochondria is essential for mitochondrial fission. The importance of Zn^{2+} was confirmed by the robust recruitment of Drp-1-GFP to mitochondria by direct delivery of Zn^{2+} through Zn-PTO (Fig. 6, E and F). Together, our data indicate that during oxidative stress, TRPM2-mediated mobilisation of lysosomal Zn^{2+} to mitochondria promotes Drp-1 recruitment and subsequent mitochondrial fragmentation.

In summary, we described a signalling pathway by which oxidative stress causes mitochondrial fragmentation (fig. S10). We showed that plasma membrane TRPM2 channels responded to oxidative stress to generate Ca^{2+} signals, which induced lysosomal membrane permeabilisation leading to the mobilisation of lysosomal Zn^{2+} to mitochondria, where Zn^{2+} promotes Drp-1 recruitment and mitochondrial fission. For Drp-1 to catalyse fission, ER tubules need to wrap around and pre-constrict the mitochondria. In this study, we found that in addition to the ER, plasma membrane and lysosomes play crucial roles in transmitting oxidative stress signals to mitochondria. Thus our study illustrates how the interplay between various organelles, in conjunction with Ca^{2+} and Zn^{2+} signals, regulates mitochondrial dynamics. Furthermore, our study raises several questions. First, how is lysosomal Zn^{2+} mobilised to mitochondria? Does it require close proximity of lysosomes to mitochondria? Second, what is the molecular route through which Zn^{2+} enters mitochondria? Third, how does Zn^{2+} promote mitochondrial Drp-1 recruitment? Does Zn^{2+} influence post-translational modifications of Drp-1 (*8, 9, 18*) required for its recruitment to mitochondria? Or does it affect other aspects of mitochondrial fission, such as ER-assisted constriction (*20*) or the recruitment of dynamin-2 (*46*)?. Notwithstanding these questions, given the growing recognition that abnormal mitochondrial fragmentation is a recurring theme in the pathophysiology of various late-onset human diseases, the findings presented in this study

may have translational potential for age-related illnesses in which mitochondrial dynamics plays a crucial role.

MATERIALS AND METHODS

Reagents and plasmid constructs

LysoTracker® Red DND-99, MitoTracker® Red CMXROS, Opti-MEM®, Pluronic®F127, Fura-2-AM, Fluo-4-AM and Fluozin3™-AM, Hoechst 33342, H2DCFDA and Lipofectamine® 2000 were purchased from Life Technologies™. DAPI (4,6-diamidino-2-phenylindole)-Fluoromount-G™ was purchased from Southern Biotech. Human TRPM2-siRNA (ON-TARGETplus Human TRPM2 (7226)) was from Thermo Scientific. TRPM2 siRNA-2 (5′-GAAAGAAUGCGUGUAUUUUGUAA -3′) was custom-made by Dharmacon. Scrambled siRNA was from Ambion (4390846). SiRNA for Drp-1 (Cat no. S1I02661365, 5'-CAGGAGCCAGCTAGATATTAA-3'), Fis-1 (Cat. No. SI04356751 5'-AAGGCCATGAAGAAAGATGGA-3') and MFF (Cat no. SI04320386, 5'-AACGCTGACCTGGAACAAGGA-3') were from Qiagen . All other chemicals were either from Sigma-Aldrich® or Calbiochem. Stock solution of zinc pyrithione was prepared by mixing aqueous solution of $ZnCl_2$ with pyrithione made up in ethanol. pMito-Cherry was constructed from pECFP-Mito (Clontech). Drp-1-GFP clone containing shRNA to knock-down the endogenous Drp-1, and its dominant negative (K38A) version (*22*), was a kind gift from Dr S Strack, University of Iowa.

Isolation of lung endothelial cells

Mice were killed by cervical dislocation. Lung microvascular endothelial cells (lung ECs) were isolated from 8-10 week old wild-type (C57BL/6) and TRPM2 knock-out (TRPM2 KO) male mice by immunoselection with anti-CD146 antibody coated magnetic beads (Miltenyi Biotec) according to the protocol described previously (*47*). Generation of TRPM2 KO mice has been described (*31*). Mice were bred and maintained under UK Home Office licence and ethical procedure.

Cell culture and transfections

Freshly isolated lung endothelial cells and human umbilical vein endothelial cells (HUVECs; Lonza) were grown in the EGM-2 medium ((Endothelial cell Basal Medium-2 (EBM-2) supplemented with endothelial growth supplements (Lonza)). The medium was changed every 24 and 48 hr for lung endothelial cells and HUVECs respectively. For experiments, lung endothelial cells were seeded onto 1:500 fibronectin (F114, Sigma) coated coverslips and HUVECs onto 0.1% gelatin coated glass bottomed dishes (35 mm FluoroDish™) and

grown in the EGM-2 medium. HUVECs were used within passage 3-6. HEK293 cells expressing tetracycline-inducible human TRPM2 (HEK293-TRPM2^{tet} cells) (*31*) were cultured in Dulbecco's modified Eagle medium (DMEM with GlutaMAX, Invitrogen) supplemented with 10% foetal bovine serum (Sigma), 50 units/ml penicillin, and 50 µg/ml streptomycin, 200 µg/ml Zeocin and 0.4 µg/ml blasticidin (InvivoGen). To induce TRPM2 expression, cells were incubated for 48 hr with 1 µg/ml tetracycline. All cells were grown at 37ºC under 5% CO_2 and humidified atmosphere.

HUVECs were grown on FluoroDish^{TM} dishes to 50-70% confluency. Cells were transfected with Drp1-GFP or pMito-Cherry using Lipofectamine 2000. Where appropriate co-transfections were performed with 25 nM human TRPM2 siRNA or scrambled siRNA. Medium was replaced 7 hr after transfection, and incubation continued for 48 to 72 hr during which cells were treated as required before imaging.

Immunostaining

For immunostaining experiments, cells were grown on coverslips. Following the desired treatments (see figure legends), cells were washed with PBS, fixed with 2% PFA (10 min) and permeabilised with 0.25% Triton X-100/10 mM Tris/150 mM NaCl, pH7.4 (5 min). Nonspecific binding sites were blocked with 1% ovalbumin/PBS for 1 hr before incubation for 2 hr with rabbit antibody against CD31 (1:300; Abcam) diluted in 1% ovalbumin/PBS. After washing thrice with PBS, cells were incubated in the dark with Alexa Fluor^{488} conjugated donkey antibody against rabbit IgG (1:500; Life Technologies) diluted in 1% ovalbumin/PBS. After washing, cover slips were mounted onto microscope slides in DAPI-Fluoromount-G and imaged.

Intracellular Zn^{2+} redistribution

Intracellular distribution of Zn^{2+} was assessed by live imaging after staining the cells with FluoZin-3 for Zn^{2+} and organelles with vital stains (*31*). HUVECs grown on FluoroDish^{TM} dishes were washed with EBM-2 medium and incubated at 37°C for 4 hr in the dark in EBM-2 containing 1 µM FluoZin-3-AM and 0.02% (w/v) Pluronic F-127. Cells were then washed twice (15 min each) with EBM-2 and incubated at 37°C for 30 min with organelle marker dyes: MitoTracker Red CMXROS (200 nM) or LysoTracker Red DND-99 (200 nM) diluted in EBM-2. After washing with EBM-2, cells were imaged. HEK-293 cells were similarly loaded, but using the relevant medium.

To examine the effect of glucose, HUVECs were incubated in EGM-2 (5.6 mM glucose) or EGM-2 containing 33 mM glucose, or 5.6 mM glucose plus 27.4 mM mannitol for 42 hr at 37°C. Cells were then loaded with FluoZin-3-AM and organelle markers in the respective

media as described above. The total incubation time including all steps was 48 hr. For ionophore mediated Zn^{2+} loading, cells were incubated in EGM-2 or EGM-2 containing 0.7 μM $ZnCl_2$ plus 0.5 μM pyrithione for 2 hr at 37°C, prior to washing and loading FluoZin-3-AM (2 hr) and organelle markers. Where appropriate, cells were co-treated with TRPM2 channel inhibitors or metal chelators, or pre-transfected with siRNA (see relevant figure legends for details). Images were captured at 37ºC using Zeiss LSM700 confocal microscope fitted with a 63× oil objective. Co-localisation of Zn^{2+} fluorescence and organelle fluorescence was determined using the Imaris software.

Mitochondrial fragmentation

Morphology of mitochondria was assessed from images of cells stained with MitoTracker Red or transfected with p-Mito-Cherry. Aspect ratio (ratio between the major and minor axis) and form factor (degree of branching) were determined using NIH ImageJ 1.44p from individual mitochondria after reducing nonspecific noise of the fluorescence signal as reported previously (*48*). Form foctor is defined as $((Perimeter^2)/(4\pi*Area))$. Mitochondrial morphology measurements were made from over 70 individual mitochondria of cells sampled from from 3 independent experiments. Mitochondria were counted as fragmented if the form factor was below 2.5. A cell is considered as its mitochondria fragmented when ≥ 50% of its total number of mitochondria is fragmented (*49*).

Drp-1 recruitment to mitochondria

To examine high glucose-induced Drp-1 recruitment to mitochondria, cells were transfected with Drp1-GFP or DN-Drp1 (K38A)-GFP with and without human TRPM2 siRNA or scrambled siRNA. 48 hrs post-transfection, cells were incubated in EGM-2 or EGM-2 containing desired additives for a further 24 hr period. Cells were then stained with MitoTracker Red, washed and imaged in EBM-2 for Drp1-GFP and MitoTracker Red.

ROS measurement

Total ROS was determined by staining cells with the H2DCFDA reagent. Cells grown in a 96 well plate were treated or not treated (control) with the test substances (see relevant figure legends). They were then incubated with 10 μM H2DCFDA diluted in EBM-2 for 30 min at 37˚C followed by three washes with EBM-2. Cells were imaged using *EVOS® FL* Cell Imaging System (Life technologies) fitted with a 40× lens. Images were analysed with Image J software. The results were expressed as the mean fluorescence intensity/cell.

Image acquisition and analysis

Images were collected with a LSM700 Zeiss inverted laser scanning confocal microscope equipped with an oil-immersion 63×/ NA 1.3 objective lens. DAPI (345 nm excitation, 458

emission) was excited with a diode laser at 405 nm, fitted with a 420-440 nm emission filter. MitoTracker Red, LysoTracker Red, Mito-Cherry (548 nm excitation, 562 nm emission) were excited using a He-Ne laser fitted with 543 nm filters. Alexa Fluor^{488} and FluoZin-3 (494 nm excitation, 519 nm emission) were excited with an Argon laser at 488 nm, fitted with a 500-530 nm emission filter. Images were acquired with ZEN lite 2011 and analysed using Image J/Imaris software. Some images were collected using iSIM (instant Structured Illumination Microscope) fitted with a Olympus Water Immersion Objective 60x/1.2 NA Uplsapo 60xw, and 488 nm and 561 nm lasers(*39*).

Intracellular Ca^{2+} measurements

Intracellular changes in [Ca^{2+}] were monitored using Fura-2-AM (*30*). HUVECs grown in 96 well plates, were incubated with Fura-2-AM (2 μM) in SBS containing 0.02% Pluronic F-127 for 1 hr at 37°C. After washing twice with SBS (10 mM HEPES, 130 mM NaCl, 1.2 mM KCl, 8 mM glucose, 1.5 mM $CaCl_2$, 1.2 mM $MgCl_2$, pH 7.4) for 30 min, 200 μl of SBS was added to each well. Fluorescence was recorded using the Flexstation® II multi-mode microplate reader (Molecular Devices, California, USA). Fluorescence was measured at 5-10 s intervals using excitation wavelengths of 340 and 380 nm and an emission wavelength of 510 nm for Ca^{2+}. After taking several control measurements, 50 μl of the desired reagents made up at 5-fold the required final concentration were added to wells. Ratio of fluorescence intensities at 340 and 380 nm (F340/F380) was calculated. For imaging cells were loased with Fluo-4-AM (1 μM) and images were collected with *EVOS® FL* Cell Imaging System (Life technologies).

Data analysis

Co-localisation analysis was performed using the Imaris software (Bitplane). Image J was used for quantification of mitochondrial morphology, Zn^{2+} uptake by mitochondria and ROS levels. All experiments were performed at least 3 times (n) and the values presented as mean ± SEM; n/N in figure legends indicate the number of independent experiments (n) over the number of cells (N) analysed. Statistical significance was assessed using the Student's *t*-test or One-way Anova, followed by Tukey post-hoc test. Probability (*P*) values are indicated with ∗, ∗∗, ∗∗∗, ∗∗∗∗ which correspond to values of 0.05, 0.01, 0.001 and 0.0001 respectively.

SUPPLEMENTARY MATERIALS

Fig. S1 TRPM2 channels mediate mitochondrial fragmentation.

Fig. S2 SOCE channels do not contribute to high glucose-induced mitochondrial fragmentation.

Fig. S3 Genetic deficiency of TRPM2 prevents high glucose-induced mitochondrial fragmentation in endothelial cells of intact aorta.

Fig. S4 Zn^{2+} chelation prevents H_2O_2-induced mitochondrial fragmentation.

Fig. S5 Ca^{2+} and Zn^{2+} ionophores induce mitochondrial fragmentation independently of TRPM2.

Fig. S6 Activation of TRPM2 channels reduces the number of lysosomes.

Fig. S7 H_2O_2-induced lysosomal permeabilization and release of cathepsin B.

Fig. S8 Extracellular Zn^{2+} does not contribute to the H_2O_2-induced increase in mitochondrial Zn^{2+} and mitochondrial fragmentation.

Fig. S9 H_2O_2-induced increase in mitochondrial Zn^{2+} is TRPM2 dependent.

Fig. S10 Signaling cascade associated with oxidative stress-induced mitochondrial fragmentation.

REFERENCES AND NOTES

1. M. Brownlee, Biochemistry and molecular cell biology of diabetic complications. *Nature* **414**, 813-820 (2001); published online EpubDec 13 (10.1038/414813a).
2. A. D. Deshpande, M. Harris-Hayes, M. Schootman, Epidemiology of diabetes and diabetes-related complications. *Phys Ther* **88**, 1254-1264 (2008); published online EpubNov (10.2522/ptj.20080020).
3. E. Orgel, S. D. Mittelman, The links between insulin resistance, diabetes, and cancer. *Curr Diab Rep* **13**, 213-222 (2013); published online EpubApr (10.1007/s11892-012-0356-6).
4. C. J. Rhodes, Type 2 diabetes-a matter of beta-cell life and death? *Science* **307**, 380-384 (2005); published online EpubJan 21 (10.1126/science.1104345).
5. D. Mathis, L. Vence, C. Benoist, beta-Cell death during progression to diabetes. *Nature* **414**, 792-798 (2001); published online EpubDec 13 (10.1038/414792a).
6. B. B. Lowell, G. I. Shulman, Mitochondrial dysfunction and type 2 diabetes. *Science* **307**, 384-387 (2005); published online EpubJan 21 (10.1126/science.1104343).
7. Y. Yoon, C. A. Galloway, B. S. Jhun, T. Yu, Mitochondrial dynamics in diabetes. *Antioxidants & redox signaling* **14**, 439-457 (2011); published online EpubFeb 1 (10.1089/ars.2010.3286).
8. S. L. Archer, Mitochondrial dynamics--mitochondrial fission and fusion in human diseases. *N Engl J Med* **369**, 2236-2251 (2013); published online EpubDec 5 (10.1056/NEJMra1215233).
9. J. R. Friedman, J. Nunnari, Mitochondrial form and function. *Nature* **505**, 335-343 (2014); published online EpubJan 16 (10.1038/nature12985).
10. M. A. Kluge, J. L. Fetterman, J. A. Vita, Mitochondria and endothelial function. *Circulation research* **112**, 1171-1188 (2013); published online EpubApr 12 (10.1161/CIRCRESAHA.111.300233).
11. A. J. Molina, J. D. Wikstrom, L. Stiles, G. Las, H. Mohamed, A. Elorza, G. Walzer, G. Twig, S. Katz, B. E. Corkey, O. S. Shirihai, Mitochondrial networking protects beta-cells from nutrient-induced apoptosis. *Diabetes* **58**, 2303-2315 (2009); published online EpubOct (10.2337/db07-1781).
12. S. M. Shenouda, M. E. Widlansky, K. Chen, G. Xu, M. Holbrook, C. E. Tabit, N. M. Hamburg, A. A. Frame, T. L. Caiano, M. A. Kluge, M. A. Duess, A. Levit, B. Kim, M. L. Hartman, L. Joseph, O. S. Shirihai, J. A. Vita, Altered mitochondrial dynamics

contributes to endothelial dysfunction in diabetes mellitus. *Circulation* **124**, 444-453 (2011); published online EpubJul 26 (10.1161/CIRCULATIONAHA.110.014506).
13. H. F. Jheng, P. J. Tsai, S. M. Guo, L. H. Kuo, C. S. Chang, I. J. Su, C. R. Chang, Y. S. Tsai, Mitochondrial fission contributes to mitochondrial dysfunction and insulin resistance in skeletal muscle. *Mol Cell Biol* **32**, 309-319 (2012); published online EpubJan (10.1128/MCB.05603-11).
14. P. M. Rappold, M. Cui, J. C. Grima, R. Z. Fan, K. L. de Mesy-Bentley, L. Chen, X. Zhuang, W. J. Bowers, K. Tieu, Drp1 inhibition attenuates neurotoxicity and dopamine release deficits in vivo. *Nat Commun* **5**, 5244 (2014)10.1038/ncomms6244).
15. J. Rehman, H. J. Zhang, P. T. Toth, Y. Zhang, G. Marsboom, Z. Hong, R. Salgia, A. N. Husain, C. Wietholt, S. L. Archer, Inhibition of mitochondrial fission prevents cell cycle progression in lung cancer. *FASEB J* **26**, 2175-2186 (2012); published online EpubMay (10.1096/fj.11-196543).
16. E. Schrepfer, L. Scorrano, Mitofusins, from Mitochondria to Metabolism. *Molecular cell* **61**, 683-694 (2016); published online EpubMar 3 (10.1016/j.molcel.2016.02.022).
17. J. Zhao, J. Zhang, M. Yu, Y. Xie, Y. Huang, D. W. Wolff, P. W. Abel, Y. Tu, Mitochondrial dynamics regulates migration and invasion of breast cancer cells. *Oncogene* **32**, 4814-4824 (2013); published online EpubOct (10.1038/onc.2012.494).
18. R. J. Youle, A. M. van der Bliek, Mitochondrial fission, fusion, and stress. *Science* **337**, 1062-1065 (2012); published online EpubAug 31 (10.1126/science.1219855).
19. T. Yu, S. S. Sheu, J. L. Robotham, Y. Yoon, Mitochondrial fission mediates high glucose-induced cell death through elevated production of reactive oxygen species. *Cardiovasc Res* **79**, 341-351 (2008); published online EpubJul 15 (10.1093/cvr/cvn104).
20. J. R. Friedman, L. L. Lackner, M. West, J. R. DiBenedetto, J. Nunnari, G. K. Voeltz, ER tubules mark sites of mitochondrial division. *Science* **334**, 358-362 (2011); published online EpubOct 21 (10.1126/science.1207385).
21. G. M. Cereghetti, A. Stangherlin, O. Martins de Brito, C. R. Chang, C. Blackstone, P. Bernardi, L. Scorrano, Dephosphorylation by calcineurin regulates translocation of Drp1 to mitochondria. *Proceedings of the National Academy of Sciences of the United States of America* **105**, 15803-15808 (2008); published online EpubOct 14 (10.1073/pnas.0808249105).
22. A. M. Slupe, R. A. Merrill, K. H. Flippo, M. A. Lobas, J. C. Houtman, S. Strack, A calcineurin docking motif (LXVP) in dynamin-related protein 1 contributes to mitochondrial fragmentation and ischemic neuronal injury. *The Journal of biological chemistry* **288**, 12353-12365 (2013); published online EpubApr 26 (10.1074/jbc.M113.459677).
23. N. Takahashi, D. Kozai, R. Kobayashi, M. Ebert, Y. Mori, Roles of TRPM2 in oxidative stress. *Cell calcium* **50**, 279-287 (2011); published online EpubSep (10.1016/j.ceca.2011.04.006).
24. A. Sumoza-Toledo, R. Penner, TRPM2: a multifunctional ion channel for calcium signalling. *The Journal of physiology* **589**, 1515-1525 (2011); published online EpubApr 1 (10.1113/jphysiol.2010.201855).
25. B. A. Miller, J. Y. Cheung, TRPM2 protects against tissue damage following oxidative stress and ischaemia-reperfusion. *The Journal of physiology* **594**, 4181-4191 (2016); published online EpubAug 1 (10.1113/JP270934).
26. C. M. Hecquet, M. Zhang, M. Mittal, S. M. Vogel, A. Di, X. Gao, M. G. Bonini, A. B. Malik, Cooperative interaction of trp melastatin channel transient receptor potential (TRPM2) with its splice variant TRPM2 short variant is essential for endothelial cell apoptosis. *Circulation research* **114**, 469-479 (2014); published online EpubJan 31 (10.1161/CIRCRESAHA.114.302414).
27. E. Fonfria, I. C. Marshall, C. D. Benham, I. Boyfield, J. D. Brown, K. Hill, J. P. Hughes, S. D. Skaper, S. McNulty, TRPM2 channel opening in response to oxidative stress is dependent on activation of poly(ADP-ribose) polymerase. *British journal of*

pharmacology **143**, 186-192 (2004); published online EpubSep (10.1038/sj.bjp.0705914).
28. J. Li, R. M. Cubbon, L. A. Wilson, M. S. Amer, L. McKeown, B. Hou, Y. Majeed, S. Tumova, V. A. Seymour, H. Taylor, M. Stacey, D. O'Regan, R. Foster, K. E. Porter, M. T. Kearney, D. J. Beech, Orai1 and CRAC channel dependence of VEGF-activated Ca2+ entry and endothelial tube formation. *Circulation research* **108**, 1190-1198 (2011); published online EpubMay 13 (10.1161/CIRCRESAHA.111.243352).
29. T. Yu, J. L. Robotham, Y. Yoon, Increased production of reactive oxygen species in hyperglycemic conditions requires dynamic change of mitochondrial morphology. *Proceedings of the National Academy of Sciences of the United States of America* **103**, 2653-2658 (2006); published online EpubFeb 21 (10.1073/pnas.0511154103).
30. F. Li, N. Abuarab, A. Sivaprasadarao, Reciprocal regulation of actin cytoskeleton remodelling and cell migration by Ca2+ and Zn2+: role of TRPM2 channels. *Journal of cell science* **129**, 2016-2029 (2016); published online EpubMay 15 (10.1242/jcs.179796).
31. P. T. Manna, T. S. Munsey, N. Abuarab, F. Li, A. Asipu, G. Howell, A. Sedo, W. Yang, J. Naylor, D. J. Beech, L. H. Jiang, A. Sivaprasadarao, TRPM2 mediated intracellular Zn2+ release triggers pancreatic beta cell death. *The Biochemical journal* **466**, 537-546 (2015); published online EpubJan 6 (10.1042/BJ20140747).
32. P. Yu, Q. Wang, L. H. Zhang, H. C. Lee, L. Zhang, J. Yue, A cell permeable NPE caged ADP-ribose for studying TRPM2. *PLoS One* **7**, e51028 (2012)10.1371/journal.pone.0051028).
33. S. L. Sensi, P. Paoletti, A. I. Bush, I. Sekler, Zinc in the physiology and pathology of the CNS. *Nat Rev Neurosci* **10**, 780-791 (2009); published online EpubNov (10.1038/nrn2734).
34. J. R. Hom, J. S. Gewandter, L. Michael, S. S. Sheu, Y. Yoon, Thapsigargin induces biphasic fragmentation of mitochondria through calcium-mediated mitochondrial fission and apoptosis. *J Cell Physiol* **212**, 498-508 (2007); published online EpubAug (10.1002/jcp.21051).
35. Q. Shen, K. Yamano, B. P. Head, S. Kawajiri, J. T. Cheung, C. Wang, J. H. Cho, N. Hattori, R. J. Youle, A. M. van der Bliek, Mutations in Fis1 disrupt orderly disposal of defective mitochondria. *Mol Biol Cell* **25**, 145-159 (2014); published online EpubJan (10.1091/mbc.E13-09-0525).
36. I. Kukic, S. L. Kelleher, K. Kiselyov, Zn2+ efflux through lysosomal exocytosis prevents Zn2+-induced toxicity. *Journal of cell science* **127**, 3094-3103 (2014); published online EpubJul 15 (10.1242/jcs.145318).
37. P. Boya, K. Andreau, D. Poncet, N. Zamzami, J. L. Perfettini, D. Metivier, D. M. Ojcius, M. Jaattela, G. Kroemer, Lysosomal membrane permeabilization induces cell death in a mitochondrion-dependent fashion. *The Journal of experimental medicine* **197**, 1323-1334 (2003); published online EpubMay 19 (10.1084/jem.20021952).
38. L. M. Malaiyandi, O. Vergun, K. E. Dineley, I. J. Reynolds, Direct visualization of mitochondrial zinc accumulation reveals uniporter-dependent and -independent transport mechanisms. *Journal of neurochemistry* **93**, 1242-1250 (2005); published online EpubJun (10.1111/j.1471-4159.2005.03116.x).
39. A. Curd, A. Cleasby, K. Makowska, A. York, H. Shroff, M. Peckham, Construction of an instant structured illumination microscope. *Methods* **88**, 37-47 (2015); published online EpubOct 15 (10.1016/j.ymeth.2015.07.012).
40. E. Smirnova, L. Griparic, D. L. Shurland, A. M. van der Bliek, Dynamin-related protein Drp1 is required for mitochondrial division in mammalian cells. *Mol Biol Cell* **12**, 2245-2256 (2001); published online EpubAug (
41. G. Szabadkai, A. M. Simoni, K. Bianchi, D. De Stefani, S. Leo, M. R. Wieckowski, R. Rizzuto, Mitochondrial dynamics and Ca2+ signaling. *Biochimica et biophysica acta* **1763**, 442-449 (2006); published online EpubMay-Jun (10.1016/j.bbamcr.2006.04.002).

42. X. J. Han, Y. F. Lu, S. A. Li, T. Kaitsuka, Y. Sato, K. Tomizawa, A. C. Nairn, K. Takei, H. Matsui, M. Matsushita, CaM kinase I alpha-induced phosphorylation of Drp1 regulates mitochondrial morphology. *The Journal of cell biology* **182**, 573-585 (2008); published online EpubAug 11 (10.1083/jcb.200802164).
43. P. Boya, G. Kroemer, Lysosomal membrane permeabilization in cell death. *Oncogene* **27**, 6434-6451 (2008); published online EpubOct 27 (10.1038/onc.2008.310).
44. H. Appelqvist, P. Waster, K. Kagedal, K. Ollinger, The lysosome: from waste bag to potential therapeutic target. *J Mol Cell Biol* **5**, 214-226 (2013); published online EpubAug (10.1093/jmcb/mjt022).
45. U. Repnik, M. Hafner Cesen, B. Turk, Lysosomal membrane permeabilization in cell death: concepts and challenges. *Mitochondrion* **19 Pt A**, 49-57 (2014); published online EpubNov (10.1016/j.mito.2014.06.006).
46. J. E. Lee, L. M. Westrate, H. Wu, C. Page, G. K. Voeltz, Multiple dynamin family members collaborate to drive mitochondrial division. *Nature* **540**, 139-143 (2016); published online EpubOct 31 (10.1038/nature20555).
47. J. Li, B. Hou, S. Tumova, K. Muraki, A. Bruns, M. J. Ludlow, A. Sedo, A. J. Hyman, L. McKeown, R. S. Young, N. Y. Yuldasheva, Y. Majeed, L. A. Wilson, B. Rode, M. A. Bailey, H. R. Kim, Z. Fu, D. A. Carter, J. Bilton, H. Imrie, P. Ajuh, T. N. Dear, R. M. Cubbon, M. T. Kearney, K. R. Prasad, P. C. Evans, J. F. Ainscough, D. J. Beech, Piezo1 integration of vascular architecture with physiological force. *Nature* **515**, 279-282 (2014); published online EpubNov 13 (10.1038/nature13701).
48. W. J. Koopman, S. Verkaart, H. J. Visch, F. H. van der Westhuizen, M. P. Murphy, L. W. van den Heuvel, J. A. Smeitink, P. H. Willems, Inhibition of complex I of the electron transport chain causes O2-. -mediated mitochondrial outgrowth. *American journal of physiology. Cell physiology* **288**, C1440-1450 (2005); published online EpubJun (10.1152/ajpcell.00607.2004).
49. K. Trudeau, A. J. Molina, S. Roy, High glucose induces mitochondrial morphology and metabolic changes in retinal pericytes. *Investigative ophthalmology & visual science* **52**, 8657-8664 (2011); published online EpubNov 07 (10.1167/iovs.11-7934).

ACKNOWLEDGMENTS

We thank Dr M. Ludlow and Dr G. Howell, University of Leeds, for advice with data analysis using Imaris/ImageJ software. We thank Dr A. Curd and Dr R Hughes, University of Leeds, for advice with iSIM, and Dr S Strack, University of Iowa, for providing Drp-1-GFP clone.

FUNDING

This work was supported by the British Heart Foundation (PG/10/68/28528) and King Saud bin Abdulaziz University for Health Sciences, Ministry of Higher Education for Saudi Arabia for a studentship (NA).

AUTHOR CONTRIBUTIONS

A.S. and N.A. conceived the study. A.S., N.A., J.L. and L.-HJ. designed the experiments. N.A. performed the experiments. N.A. and T.M. analyzed the data. N.A. and A.S. wrote the manuscript.

COMPETING INTERESTS

The authors declare that they have no competing interests.

FIGURE LEGENDS

Fig. 1. Inhibition of TRPM2 channels prevents high glucose-induced mitochondrial fragmentation. (**A**) HUVECs expressing mitochondria-targeted mito-Cherry protein were incubated with Endothelial Cell Growth Medium-2 (EGM2) (CTRL, 5.6 mM), or EGM2 supplemented with mannitol (27.4 mM) or high glucose (27.4 mM) for 24 hrs. Where indicated, cells were co-transfected with siRNA or treated with 37.5 μM 2-APB. Representative confocal images are shown; scale bar, 10 μm. Boxed regions are magnified in the lower panels. Scale bar, 5 μm. (**B**) Plots of form factor against aspect ratio calculated from the images in A. (**C**-**D**) Mean ± SEM of aspect ratio (C) and form factor (D) calculated from the data in (A), analysed as in (B); n=3 independent experiments, N=9 cells in total. (**E**) Mean ± SEM of percent cells displaying mitochondrial fragmentation determined from data in (A); n = 3 independent experiments, N=130 cells in total. (**F**) ROS production in HUVECs following the treatments as in (A). Cells were stained with H2DCF-DA (DCF) and mean ± SEM of fluorescence per cell are presented; n = 3 independent experiments, N = 180 cells in total. (**G**) Representative confocal images of HUVECS exposed to high glucose with and without the ROS scavenger NAC. (**H**) Mean ± SEM of percent cells displaying mitochondrial fragmentation determined from the data in (G); n=3 independent experiments, N=70 cells in total. Statistical analysis was performed by one-way ANOVA with Tukey's post-hoc test. *p <0.05, **P < 0.01, ***P < 0.001, and ****P < 0.0001. NS, not significant.

Fig. 2. Knock-out of TRPM2 channels prevents high glucose-induced mitochondrial fragmentation in mouse pulmonary endothelial cells. (**A** to **F**) Effect of high glucose on mitochondrial fragmentation of primary endothelial cells isolated from wild-type (WT) mice (A to C) or TRPM2 knock-out (TRPM2 KO) mice (D to F). Cells were incubated with 5.6 mM glucose (CTRL), mannitol (27.4 mM) or high glucose (27.4 mM) for 72 hrs and stained with MitoTracker Red (red, mitochondria), rabbit antibodies against CD31 (green, endothelial cells) and DAPI (nuclei, blue). (**A** and **D**) show representative images; scale bar, 10 μM. Boxed regions in the merged images are expanded in the bottom panels; scale bar, 5 μm. (**B** and **E**) Plots of form factor against aspect ratio calculated from the images in (A) and (D) respectively. (**C and F)** Mean ± SEM of aspect ratio and form factor calculated from data analysed as in (B) and (E) respectively; (n=3 independent experiments; cells from 2-3 mice were pooled for each experiment); N=9 cells in total. (**G)** Comparison of aspect ratio and form factor of mitochondria of endothelial cells isolated from WT and TRPM2 KO mice, following various treatments (data from C and F). Statistical analysis was performed by one-

way ANOVA with Tukey's post-hoc test. *p <0.05, **P < 0.01, and ***P < 0.001. NS, not significant.

Fig. 3. High glucose-induced mitochondrial fragmentation is mediated by Zn^{2+}. (**A**) Representative images of the effect of the Zn^{2+} chelator TPEN (0.3 μM) on HUVECs expressing mito-Cherry and incubated with 5.6 mM glucose (CTRL) or high glucose (33 mM glucose). (**B** and **C**) Mean ± SEM of form factor (B) and aspect ratio (C) calculated from the data in (A); n=3 independent experiments, N=9 cells in total. (**D**) Mean ± SEM of percent cells showing mitochondrial fragmentation, calculated from the data in (A), n = 3 independent experiments, N=130 cells in total. (**E**) Representative images of the effect of delivering Zn^{2+} through pyrithione (Zn-PTO: 0.7 μM Zn^{2+}: 0.5 μM pyrithione) on HUVECs expressing mito-Cherry, in the presence or absence of TPEN (0.3 μM). (**F**) Mean ± SEM of percent cells showing mitochondrial fragmentation, calculated from the data in (E), n = 3 independent experiments, N=170 cells in total. (**G**) A23187 (1 μM) application, shown with a horizontal bar, causes an increase in cytosolic Ca^{2+} (Ca^{2+}_i). (**H**) Mean ± SEM of change in Ca^{2+} fluorescence calculated from the data in (G), n=3 independent experiments. (**I**) Representative confocal images of cells treated with vehicle (CTRL) or A23187 (1 μM) and stained for Ca^{2+}. (**J**) Representative confocal images of HUVECs treated with vehicle (CTRL) or 1 μM A23187 for the indicated times and stained for mitochondria, in the presence or absence of TPEN (0.3 μM). (**K**) Mean ± SEM of percent cells showing mitochondrial fragmentation, calculated from the data in (J); n = 3 independent experiments, N=170 cells in total. In representative confocal images, scale bar = 10 μm; in images in which boxed regions are expanded, scale bar = 5 μm. Statistical analysis was performed by one-way ANOVA with Tukey's post-hoc test (B to D, F and K) or Students t-test (H); *p <0.05, **P < 0.01 and ***P < 0.001. NS, not significant.

Fig. 4. High glucose induces lysosomal membrane permeabilisation through TRPM2 mediated Ca^{2+} rise. (**A**) Representative confocal images of HUVECs incubated with 5.6 mM glucose (CTRL), mannitol (27.4 mM) or high glucose (27.4 mM) for 24 hours and stained for Zn^{2+} (FluoZin-3; green) and lysosomes (LysoTracker Red, red). (**B**) Mean ± SEM of the percentage of LysoTracker Red-positive lysosomes per cell, calculated from the data from (A), n=3 independent experiments; N = 100 cells in total. (**C**) HEK293-$TRPM2^{tet}$ were not induced (-Tet) or induced (+Tet) with tetracycline before exposure to H_2O_2 (200 μM, 90 min) and staining for lysosomes. (**D**) Mean ± SEM of the percentage of LysoTracker Red-positive lysosomes per cell, calculated from the data from (C), n=3 independent experiments; N = 100 cells in total. (**E**) Representative confocal images of cells exposed to EGM2 alone or EGM2 supplemented with 1 μM A23187 for 2 or 4 hrs before staining with LysoTracker Red. (**F**) Mean ± SEM of the percentage of LysoTracker Red-positive lysosomes per cell,

calculated from the data in (E) (n =3 independent experiments; N = 100 cells in total). (**G**) HUVECs transfected with scrambled siRNA or TRPM2-siRNA were treated with A23187 for 4 hrs and stained as in (E). Mean ± SEM percentage of LysoTracker Red-positive lysosomes per cell from 3 independent experiments is shown; N = 100 cells in total. In representative confocal images, scale bar = 10 μm; in images in which boxed regions are expanded, scale bar = 5 μm. Statistical analysis was performed by one-way ANOVA with Tukey's post-hoc test. *p <0.05, **P < 0.01 and ***P < 0.001. NS, not significant.

Fig. 5. High glucose increases mitochondrial Zn^{2+} and fragmentation through TRPM2 channel activation. (**A**) HUVECs were incubated with 5.6 mM glucose (CTRL), mannitol (27.4 mM) or high glucose (27.4 mM) for 24 hours and stained for Zn^{2+} (FluoZin-3; green) and mitochondria (MitoTracker Red, red). Representative confocal images are shown; scale bar, 10 μm. Boxed regions in the merged images are magnified in the far right panels. Scale bar, 5 μm. (**B**) Mean ± SEM of percent localisation of Zn^{2+} with mitochondria calculated from the data in (A). N=3 independent experiments. CTRL, 155 cells; Mannitol, 91 cells; high glucose, 119 cells; scrambled (Scr) siRNA, 108 cells; siRNA-TRPM2, 148 cells. (**C**) Percentage of cells showing mitochondrial fragmentation, calculated from the data in (A), n = 3 independent experiments, N=160 cells in total. Statistical analysis for B and C was performed by one-way ANOVA with Tukey's post-hoc test, *p <0.05, **P < 0.01 and ***P < 0.001. (**D**) iSIM images of HUVECs showing localization of Zn^{2+} in mitochondria following high glucose and H_2O_2-induced stress. HUVECs expressing Mito-Cherry were treated with high glucose (33 mM, 24 hrs) or H_2O_2 (200 μM, 2 hrs) before staining for Zn^{2+} with FluoZin-3. Representative images (n = 3 independent experiments) are shown; scale bar = 10 μM.

Fig. 6. High glucose-induced TRPM2 activation and rise in Zn^{2+} promotes mitochondrial Drp-1 recruitment. (**A**) Representative confocal images of HUVECs transfected with Drp-1-GFP or dominant negative (DN)-Drp1-GFP and incubated with 5.6 mM glucose (CTRL), mannitol (27.4 mM) or high glucose (27.4 mM) for 24 hours. TPEN (0.3 μM) was included as indicated. (**B**) Mean ± SEM of percentage co-localization of GFP with MitoTracker Red calculated from the data in (A); n=3 independent experiments; N= 50 cells in total. (**C**) Representative iSIM fluorescent images of mitochondrial fragmentation in HUVECs co-transfected with pMitoCherry and siRNA targeting Drp1, Fis-1 and/or MFF and exposed to high glucose for 48 hrs. (**D**) Mean ± SEM data for percent cells with mitochondrial fragmentation from experiments performed as in (C); n = 3 independent experiments, N = 60 cells in total. (**E**) Representative confocal images of HUVECs transfected with Drp-1-GFP or DN-Drp1-GFP, treated with Zn-PTO for 1 hr and stained for mitochondria. (**F**) Mean ± SEM of percentage co-localization of GFP with MitoTracker Red,

calculated from the data in (E); n=3 independent experiments; N=50 cells in total. In representative confocal images scale bar = 10 μm. Statistical analysis was performed by one-way ANOVA with Tukey's post-hoc test, *p <0.05, **p <0.01 and ***P < 0.001.

Fig. 1

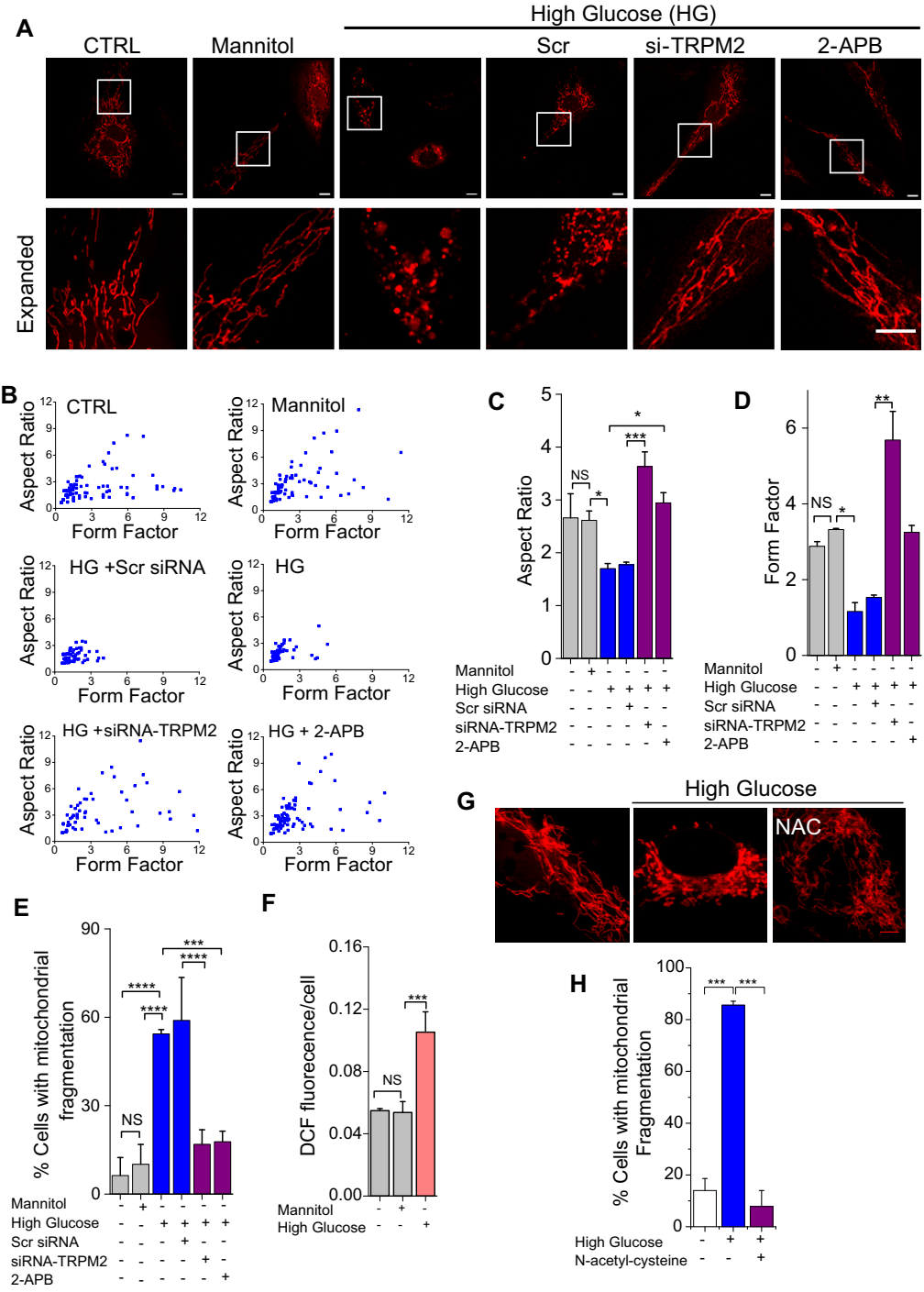
A
High Glucose (HG)
CTRL
Mannitol
Scr
si-TRPM2
2-APB
Expanded
B
CTRL
Mannitol
HG +Scr siRNA
HG
HG +siRNA-TRPM2
HG + 2-APB
Aspect Ratio
Form Factor
C
Aspect Ratio
NS
Mannitol
High Glucose
Scr siRNA
siRNA-TRPM2
2-APB
D
Form Factor
NS
Mannitol
High Glucose
Scr siRNA
siRNA-TRPM2
2-APB
E
% Cells with mitochondrial fragmentation
NS
Mannitol
High Glucose
Scr siRNA
siRNA-TRPM2
2-APB
F
DCF fluorecence/cell
NS
Mannitol
High Glucose
G
High Glucose
NAC
H
% Cells with mitochondrial Fragmentation
High Glucose
N-acetyl-cysteine

Fig. 2

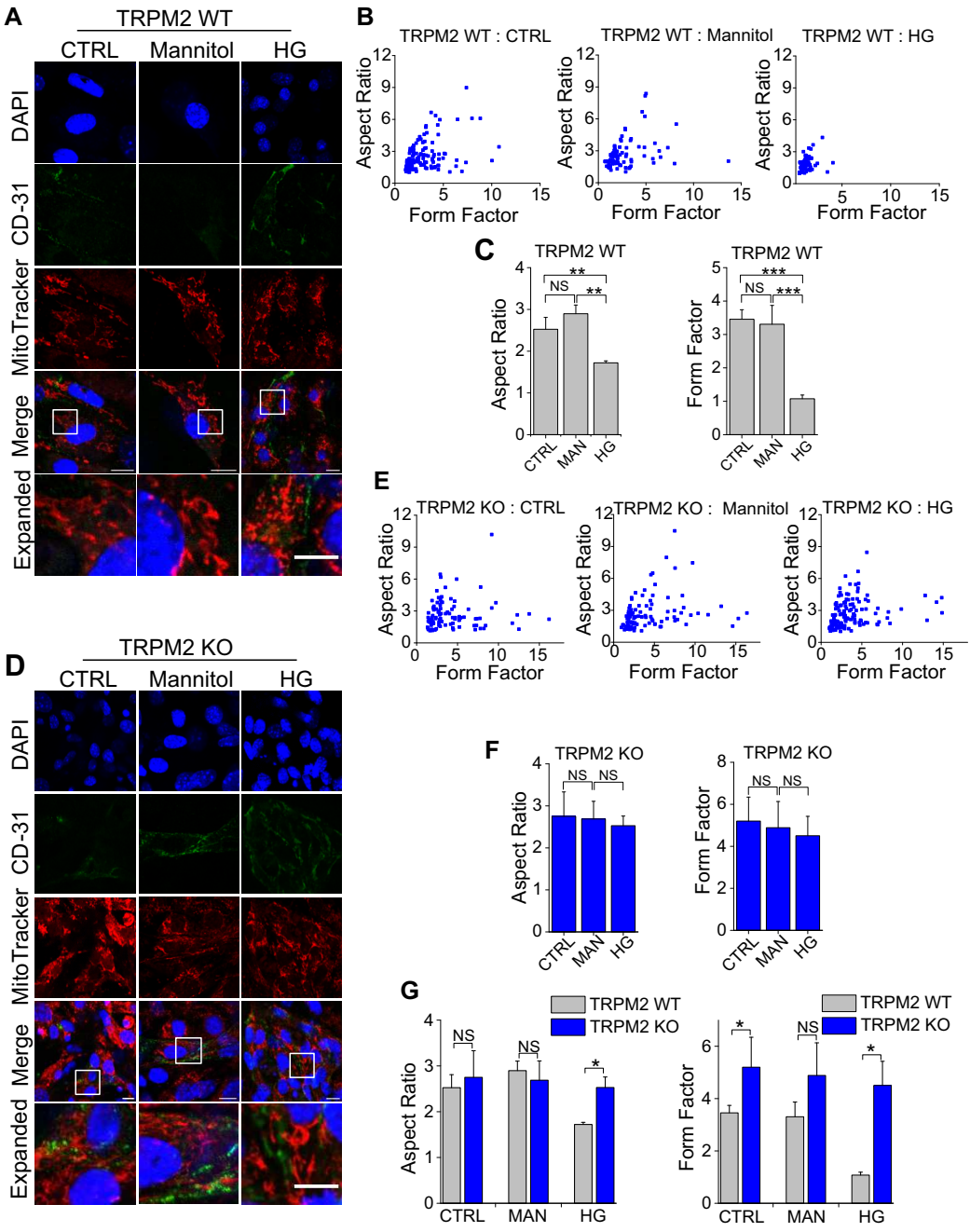
A
TRPM2 WT
CTRL
Mannitol
HG
DAPI
CD-31
MitoTracker
Merge
Expanded
D
TRPM2 KO
B
TRPM2 WT : CTRL
TRPM2 WT : Mannitol
TRPM2 WT : HG
Aspect Ratio
Form Factor
C
TRPM2 WT
NS
**
***
E
TRPM2 KO : CTRL
TRPM2 KO : Mannitol
TRPM2 KO : HG
F
TRPM2 KO
G
TRPM2 WT
TRPM2 KO
*
CTRL
MAN
HG

Fig. 3

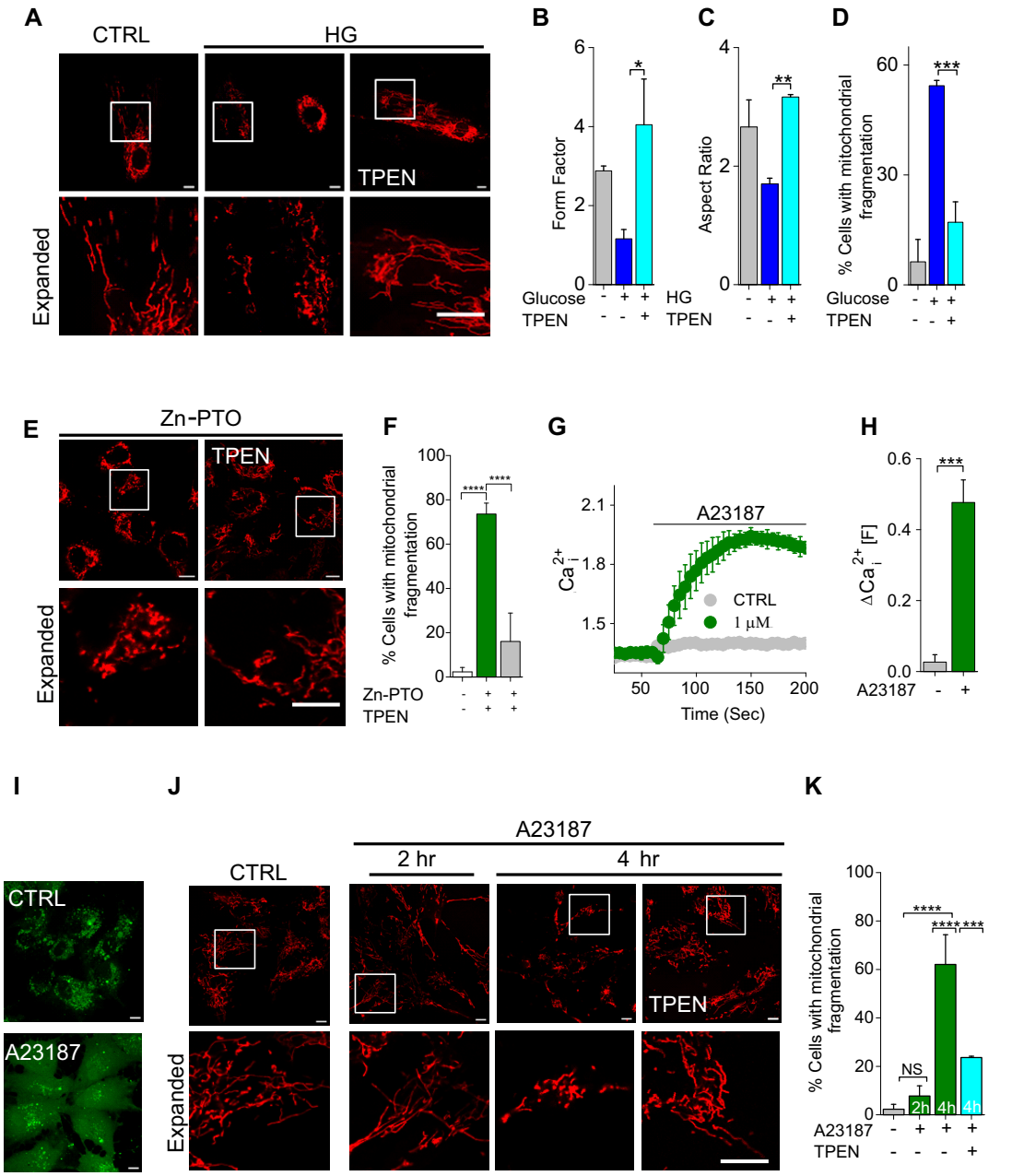
A
CTRL
HG
TPEN
Expanded
B
Form Factor
Glucose
TPEN
C
Aspect Ratio
HG
TPEN
D
% Cells with mitochondrial fragmentation
Glucose
TPEN
E
Zn-PTO
TPEN
Expanded
F
% Cells with mitochondrial fragmentation
Zn-PTO
TPEN
G
A23187
CTRL
1 μM
Time (Sec)
H
ΔCa2+i [F]
A23187
I
CTRL
A23187
J
A23187
2 hr
4 hr
CTRL
TPEN
Expanded
K
% Cells with mitochondrial fragmentation
NS
2h
4h
4h
A23187
TPEN

Fig. 4

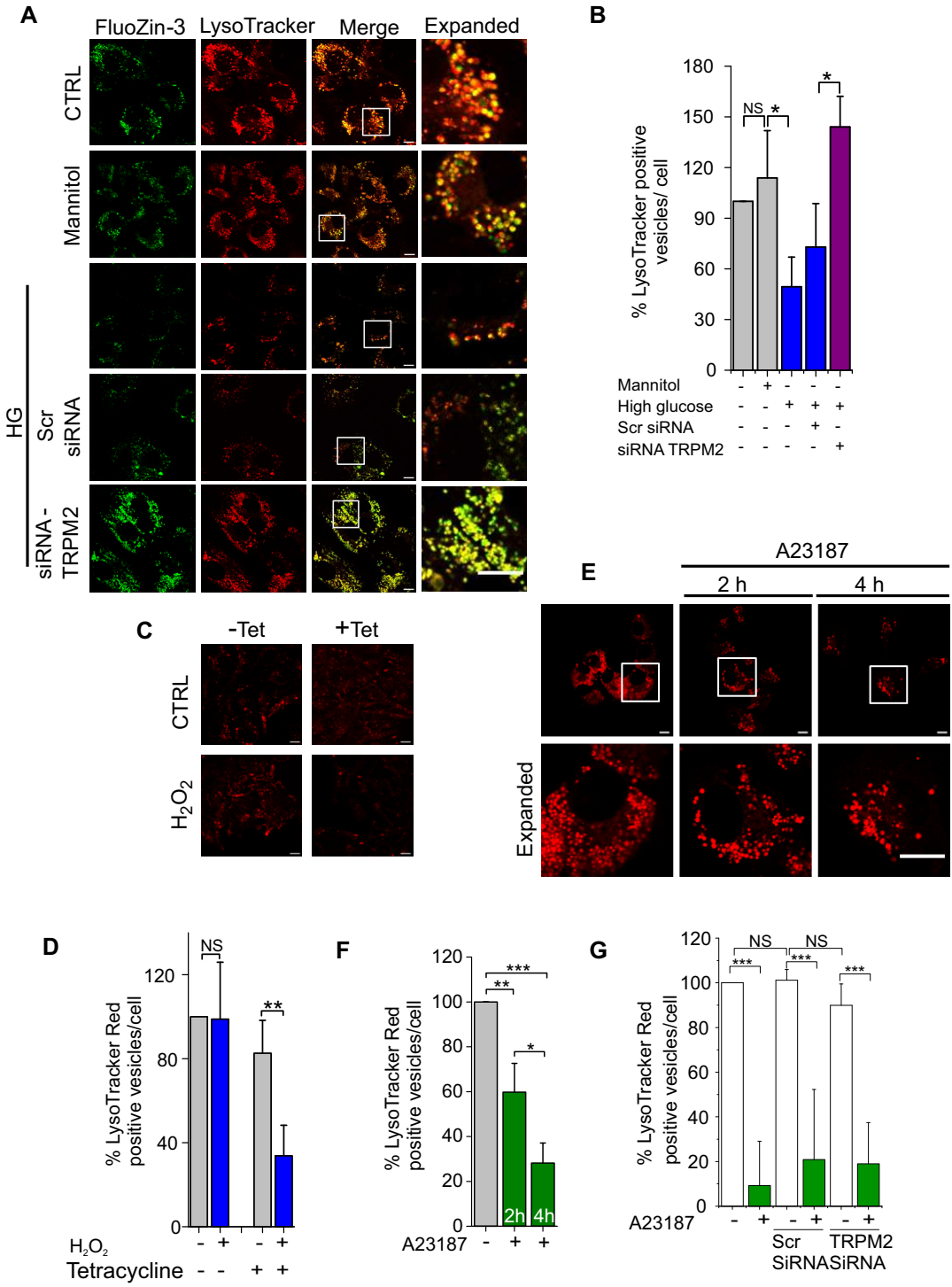
A
FluoZin-3
LysoTracker
Merge
Expanded
CTRL
Mannitol
HG
Scr siRNA
siRNA - TRPM2
B
% LysoTracker positive vesicles/ cell
NS
*
*
Mannitol
High glucose
Scr siRNA
siRNA TRPM2
C
-Tet
+Tet
CTRL
H2O2
D
% LysoTracker Red positive vesicles/cell
NS
**
H2O2
Tetracycline
E
A23187
2 h
4 h
Expanded
F
% LysoTracker Red positive vesicles/cell
***
**
*
2h
4h
A23187
G
% LysoTracker Red positive vesicles/cell
NS
NS
***
***
***
A23187
Scr SiRNA
TRPM2 SiRNA

Fig. 5

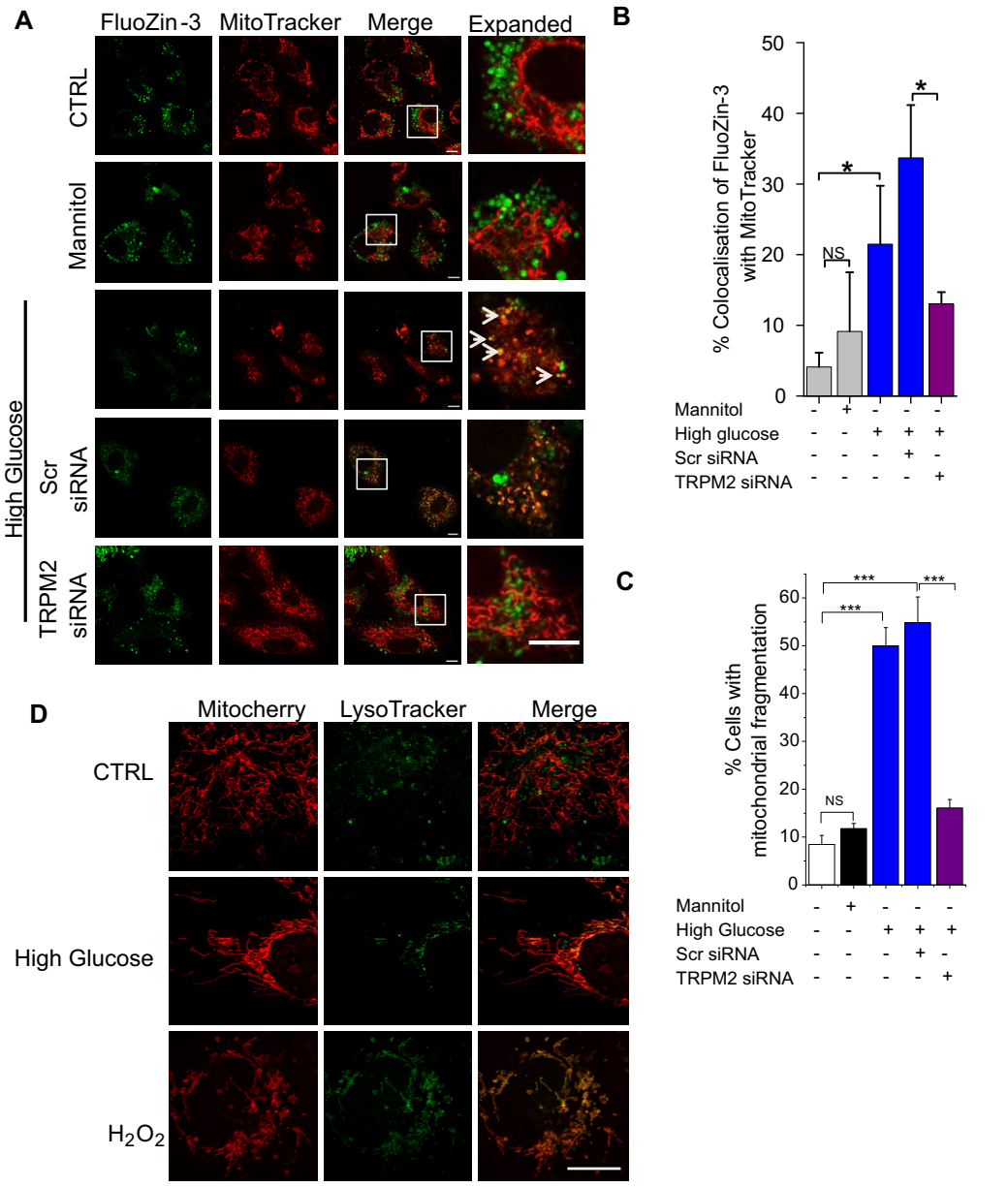
A
FluoZin-3
MitoTracker
Merge
Expanded
CTRL
Mannitol
High Glucose
Scr siRNA
TRPM2 siRNA
B
% Colocalisation of FluoZin-3 with MitoTracker
NS
*
*
Mannitol
High glucose
Scr siRNA
TRPM2 siRNA
C
% Cells with mitochondrial fragmentation
NS
***
***
***
Mannitol
High Glucose
Scr siRNA
TRPM2 siRNA
D
Mitocherry
LysoTracker
Merge
CTRL
High Glucose
H2O2

Fig. 6

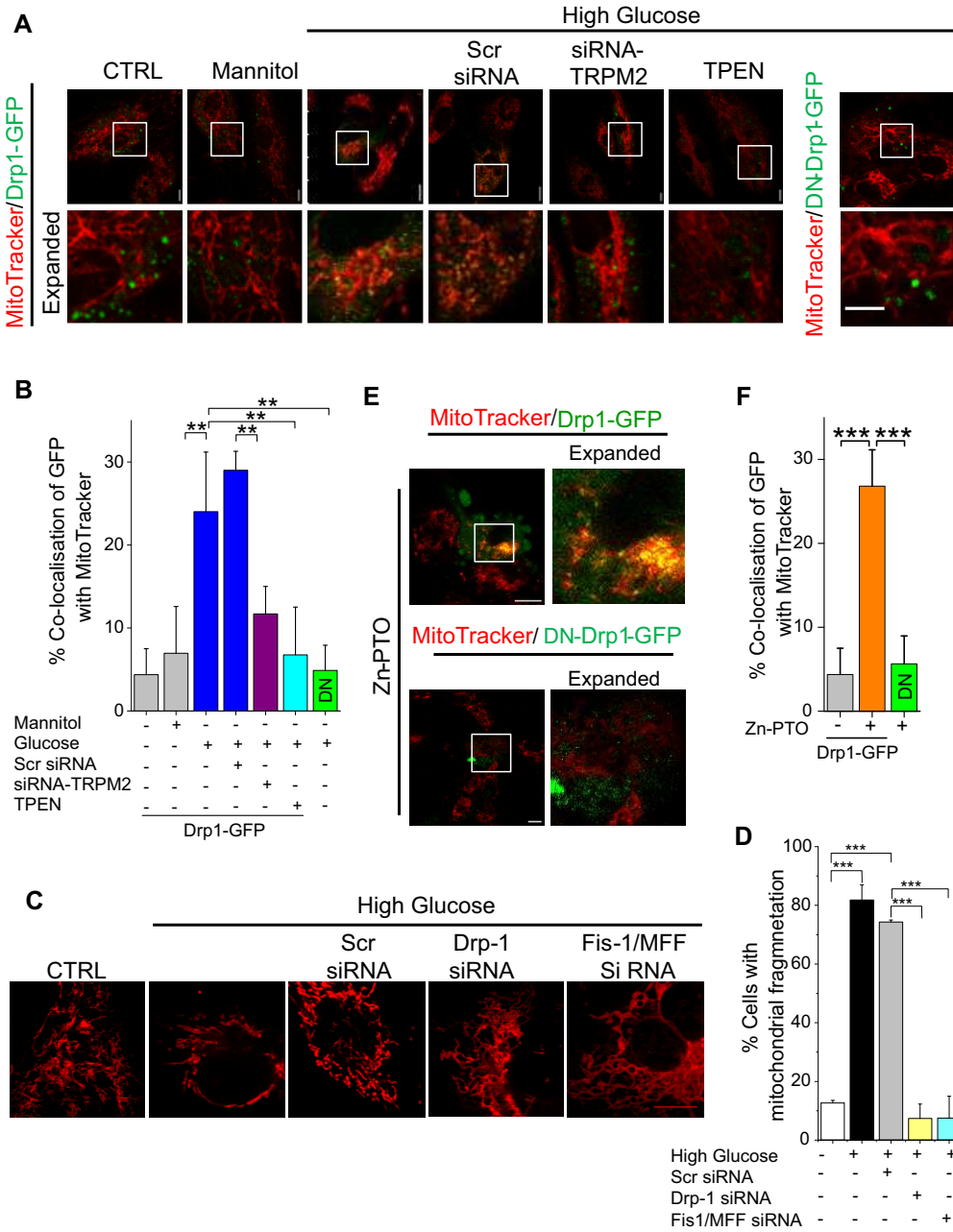
A
High Glucose
CTRL
Mannitol
Scr siRNA
siRNA-TRPM2
TPEN
MitoTracker/Drp1-GFP
Expanded
MitoTracker/DN-Drp1-GFP
B
% Co-localisation of GFP with MitoTracker
Mannitol
Glucose
Scr siRNA
siRNA-TRPM2
TPEN
DN
Drp1-GFP
C
High Glucose
CTRL
Scr siRNA
Drp-1 siRNA
Fis-1/MFF Si RNA
D
% Cells with mitochondrial fragmentation
High Glucose
Scr siRNA
Drp-1 siRNA
Fis1/MFF siRNA
E
MitoTracker/Drp1-GFP
Expanded
Zn-PTO
MitoTracker/ DN-Drp1-GFP
F
% Co-localisation of GFP with MitoTracker
Zn-PTO
Drp1-GFP

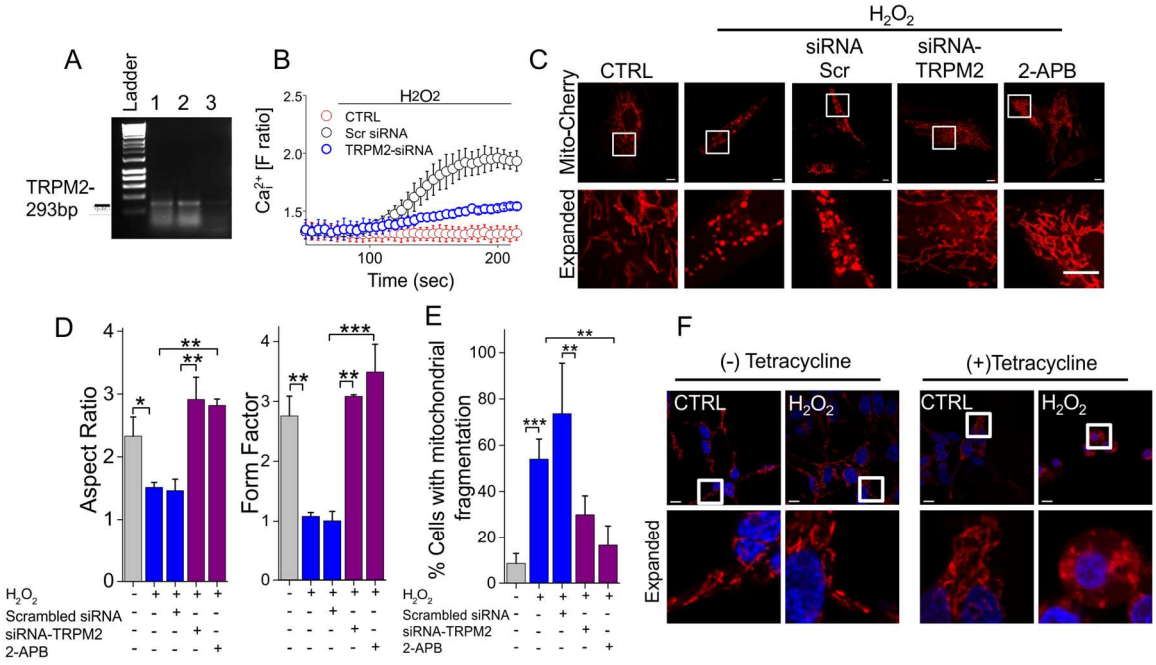

Fig. S1. TRPM2 channels mediate mitochondrial fragmentation. (**A**) Demonstration of silencing of TRPM2 mRNA expression by RNAi. Lanes 1-3: RT-PCR products from mRNA isolated from untransfected HUVECs (lane 1) or HUVECs transfected with scrambled (negative control) siRNA (lane 2) or siRNA targeted to TRPM2 (lane 3). The TRPM2 band (lane 3) is absent in TRPM2 siRNA transfected samples, but not scrambled siRNA controls (lane 2); n=2 independent experiments. (**B**) Demonstration of RNAi silencing of TRPM2 by calcium imaging. Cells transfected with scrambled siRNA or siRNA targeted to the TRPM2 channel were loaded with Fura-2-AM and the effect of 3 mM H_2O_2 application (shown with horizontal bar) on Ca^{2+} rise was recorded using FlexStation II. n=3 independent experiments. (**C**) Inhibition of TRPM2 channels prevents H_2O_2-induced mitochondrial fragmentation. HUVECs were transfected with pMito-Cherry (mitochondrial marker) and incubated with 1 mM H_2O_2 for 3 hr at 37°C in the presence and absence of a non-specific TRPM2 blocker (37.5 µM 2-APB). Cells were co-transfected with pMito-Cherry and scrambled siRNA or siRNA targeted to TRPM2 channels before exposing to 1 mM H_2O_2 for 3 hr at 37°C. Representative confocal images are shown. Scale bar, 10 µm. Boxed regions are magnified in the lower panels. Scale bar, 5 µm. (**D**) Mean ± SEM of aspect ratio and form factor calculated from experiments performed as in C; n = 3 independent experiments; N = 9 total number of cells. (**E**) Mean ± SEM of percent cells displaying mitochondrial fragmentation determined from data in C, n = 3 independent experiments, N=100 total number of cells. (**F**) HEK293-TRPM2^{tet} cells were either not induced (+tetracycline) or induced (-tetracycline) to express TRPM2 channels with tetracycline. Cells were incubated with standard buffered saline (SBS) alone (CTRL) or 200 µM H_2O_2 in SBS for 90 min and then labelled with MitoTracker Red. Representative confocal images (3 independent experiments). Scale bar, 10 µM. Boxed sections are expanded in the lower panels. Statistical significance was assessed by one-way ANOVA with Tukey's post-hoc test *p <0.05, *p <0.01 and **P < 0.001.

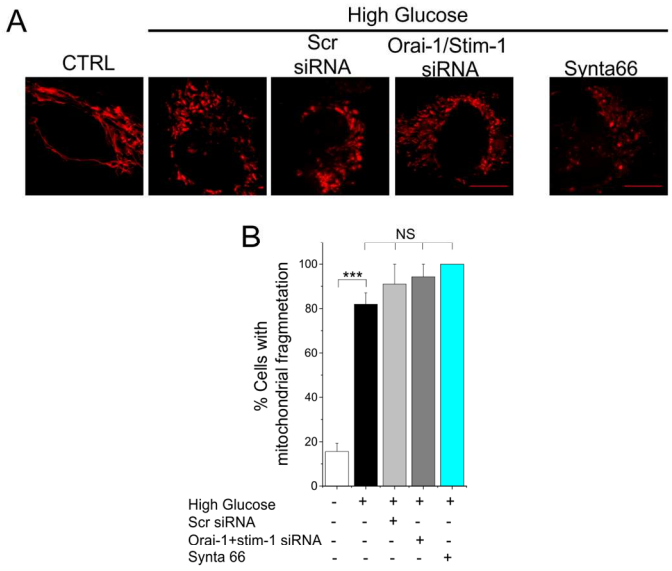

Fig. S2. SOCE channels do not contribute to high glucose-induced mitochondrial fragmentation. (**A**) HUVECs were co-transfected with pMitoCherry and scrambled siRNA or siRNA targeted to Orai-1 (GGAAGAGGAUUUUUAUAAtt; UUAUAAAAAUCCUCUUCCCtc) and Stim-1 (CAAUUCGGCAAAACUCUGCtg; GCAGAGUUUUGCCGAAUUGtt) (*28*). 24 hrs later, medium was replaced with EGM2 containing normal glucose concentration or high glucose. Cells were imaged after 48 hrs. HUVECs transfected with pMitoCherry were also incubated in EGM2 containing high glucose supplemented with 5 μM Synta 66, a specific blocker of SOCE channels (*28*). Representative iSIM fluorescent images show lack of effect of these treatments on high glucose-induced mitochondrial fragmentation. (**B**) Mean ± SEM data for percent cells with mitochondrial fragmentation from experiments performed as in (A); the data are from 3 independent experiments; N= 40 total number of cells. In the images, scale bar = 10 μm. Statistical analysis was performed by one-way ANOVA with Tukey's post-hoc test, ***$P < 0.001$; NS, not significant.

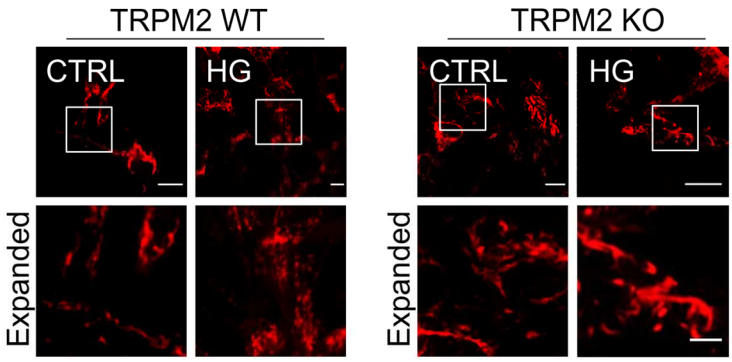

Fig. S3. Genetic deficiency of TRPM2 prevents high glucose-induced mitochondrial fragmentation in endothelial cells of intact aorta. Slices of aortas isolated from wild-type (TRPM2 WT) and TRPM2 knock-out (TRPM2 KO) mice were stained *in situ* for mitochondria with MitoTracker Red and fixed with 4% PFA. For high glucose treatment, aortas were maintained in 33 mM glucose (HG) in EGM2 medium at 37°C for 72 hrs. Images of the luminal aspect of the sections were taken using Zeiss LSM700 confocal microscope. Images are representative of sections from 3 mice per genotype and treatment. Scale bar, 10 μM. Boxed regions are magnified in the lower panels. Scale bar, 5 μm.

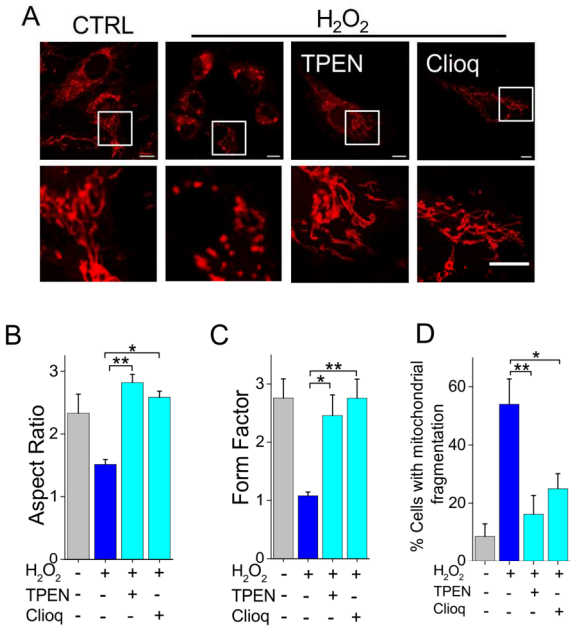

Fig. S4. Zn^{2+} chelation prevents H_2O_2-induced mitochondrial fragmentation. (**A**) HUVECs were transfected with pMito-Cherry and incubated with 1 mM H_2O_2 for 3 hr at 37°C in the presence and absence of zinc chelators (0.3 µM TPEN and 2 µM clioquinol) before imaging. Representative confocal images are shown. Scale bar, 10 µm. Boxed regions are magnified in the lower panels. Scale bar, 5 µm. (**B-C**) Mean ± SEM of aspect ratio and form factor calculated from experiments performed as in (A), n = 3 independent experiments, N = 9 total number of cells. (**D**) Mean ± SEM of percent cells displaying mitochondrial fragmentation determined from experiments performed as in **A**, n = 3 independent experiments, N=100 total number of cells. Statistical significance was assessed by one-way ANOVA with Tukey's post-hoc test *p <0.05 and **P < 0.01.

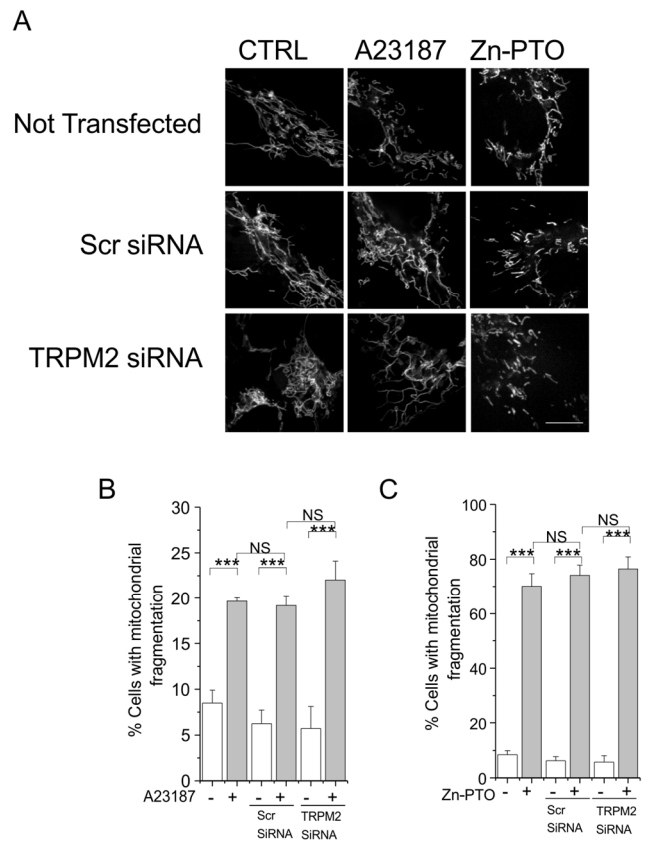

Fig. S5. Ca^{2+} and Zn^{2+} ionophores induce mitochondrial fragmentation independently of TRPM2. (**A**) HUVECs were co-transfected with pMitoCherry and scrambled siRNA or siRNA targeted to TRPM2 channels and exposed to EBM2 (CTRL) or EBM2 containing A23187 (1 μM) or Zn-PTO (1 μM) for 4 hrs before imaging. Representative iSIM fluorescent images show that both the ionophores induced mitochondrial fragmentation independently of TRPM2. (**B-C**) Mean ± SEM data for percent cells with mitochondrial fragmentation for A23187 (B) and Zn-PTO (C) from experiments performed as in (A); the data are from 3 independent experiments; N = 100 total number of cells.

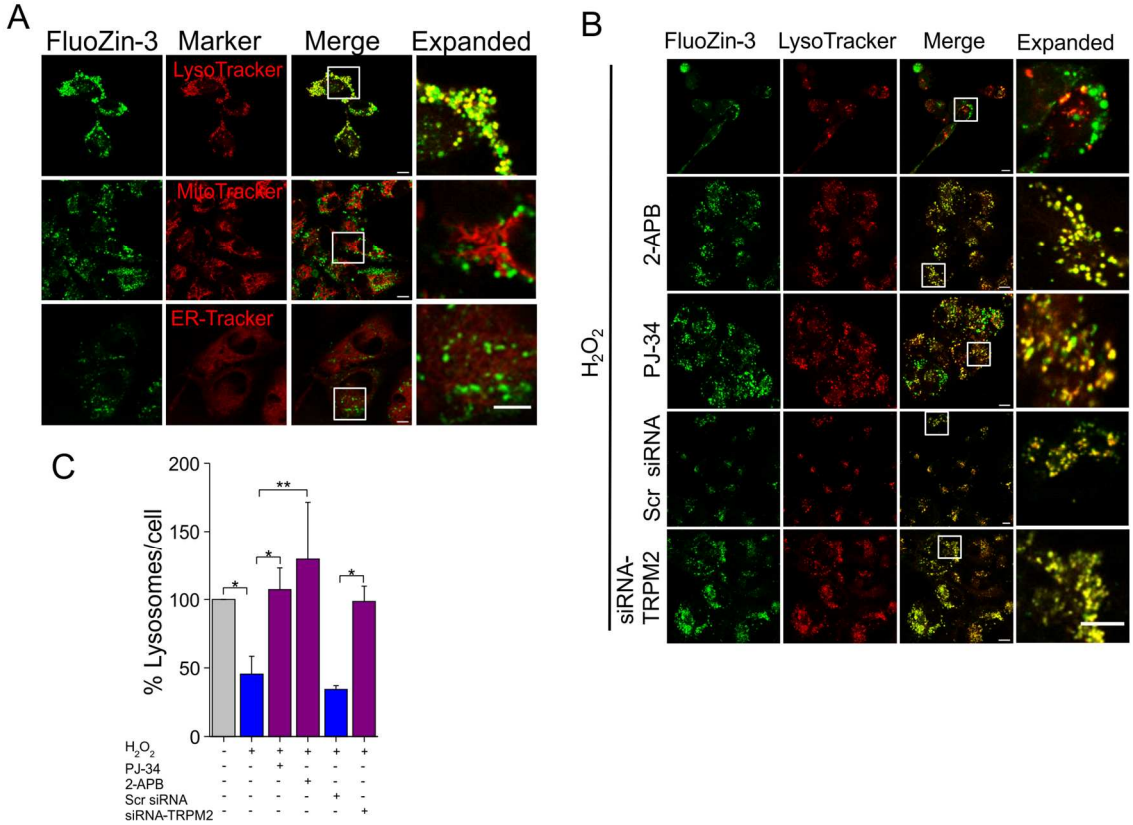

Fig. S6. Activation of TRPM2 channels reduces the number of lysosomes. (**A**) Free Zn^{2+} is largely stored in lysosomes. Fluorescence microscopy images of HUVECs co-stained for Zn^{2+} (FluoZin-3; green) and intracellular organelles (red): lysosomes (LysoTracker), mitochondria (MitoTracker Red) and the ER (ER-Tracker). Merged images show marked localisation of Zn^{2+} to lysosomes (yellow), but not to mitochondria or the ER. Zn^{2+} staining was not apparent in the cytoplasm. Scale bar, 10 µm. Boxed regions in the merged images are magnified in the far right panels. Scale bar, 5 µm. Images shown are representative from 3 independent experiments. (**B**) Inhibition of TRPM2 channels with pharmacological inhibitors and TRPM2-siRNA rescues H_2O_2 induced decrease in the lysosomal number. Live cell fluorescent images of HUVECs following exposure to 1 mM H_2O_2 (4 hr, 37°C); cells were co-treated with PJ34 (10 µM) or 2-APB (150 µM) or pre-transfected with scrambled siRNA or TRPM2-siRNA. Confocal images show FluoZin-3 and LysoTracker staining; scale bar, 10 µm. Boxed regions in the merged images are magnified in the far right panels, scale bar, 5 µm. (**C**) Mean ± SEM of data from (B) expressed as percent LysoTracker positive lysosomes per cell. n=3 independent experiments. Minus H_2O_2, 139 cells; H_2O_2, 121 cells; PJ34, 48 cells; 2-APB, 112 cells; scrambled siRNA, 91 cells; siRNA-TRPM2, 222 cells. Statistical significance was assessed by one-way ANOVA with Tukey's post-hoc test, *p <0.05, **P < 0.01.

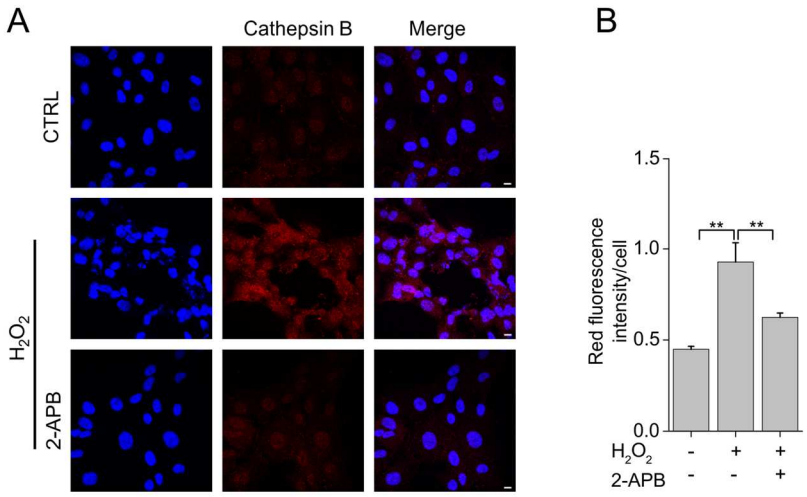

Fig. S7. H_2O_2-induced lysosomal permeabilization and release of cathepsin B. (A) HUVECs were untreated (CTRL) or treated with H_2O_2 (1 mM) in the presence and absence of 2-APB (150 μM) for 4 hours before staining for cathepsin B and the nucleus with DAPI. Cathepsin B was stained using mouse antibodies against cathepsin B (1:100; Calbiochem) and Cy-3 conjugated donkey antibodies against mouse IgG (1:500; Jackson ImmunoReseach). Representative fluorescent images are shown. Cytoplasmic staining of cathepsins B indicates LMP; inhibition by 2-ABP indicates a role for TRPM2 channels. **(B)** Mean ± SEM of fluorescence intensity per cell of cathepsin B stain estimated from ≥ 60 total number of cells, from three independent experiments.

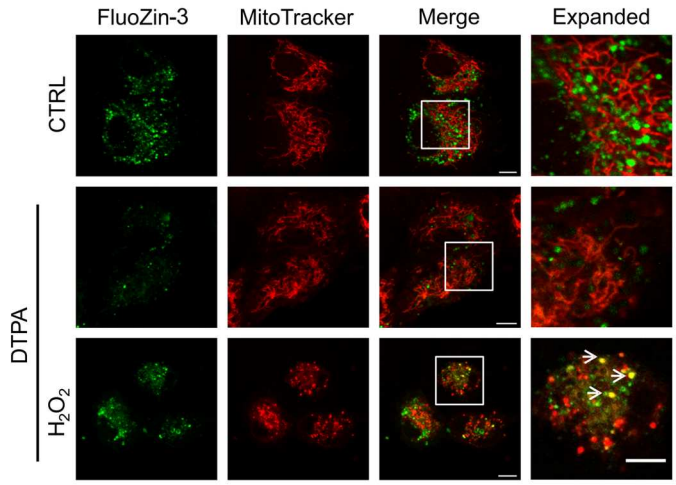

Fig. S8. Extracellular Zn^{2+} does not contribute to the H_2O_2-induced increase in mitochondrial Zn^{2+} and mitochondrial fragmentation. HUVECs were exposed for 4 hrs at 37°C to EGM2 medium alone (CTRL) or to medium containing 1 mM diethylenetriamine pentaacetate (DTPA, a membrane impermeable Zn^{2+} chelator) with and without 1 mM H_2O_2. Cells were then stained for Zn^{2+} (FluoZin-3) and mitochondria (MitoTracker Red). Merged images show that DTPA was unable to prevent H_2O_2-induced rise in mitochondrial Zn^{2+} (yellow puncta) and mitochondrial fragmentation. The results suggest that H_2O_2 causes redistribution of intracellular Zn^{2+} to mitochondria. Images are representative of 3 independent experiments. Scale bar, 10 μm. Boxed regions in the merged images are magnified in the far right panels with arrows highlighting yellow puncta. Scale bar, 5 μm.

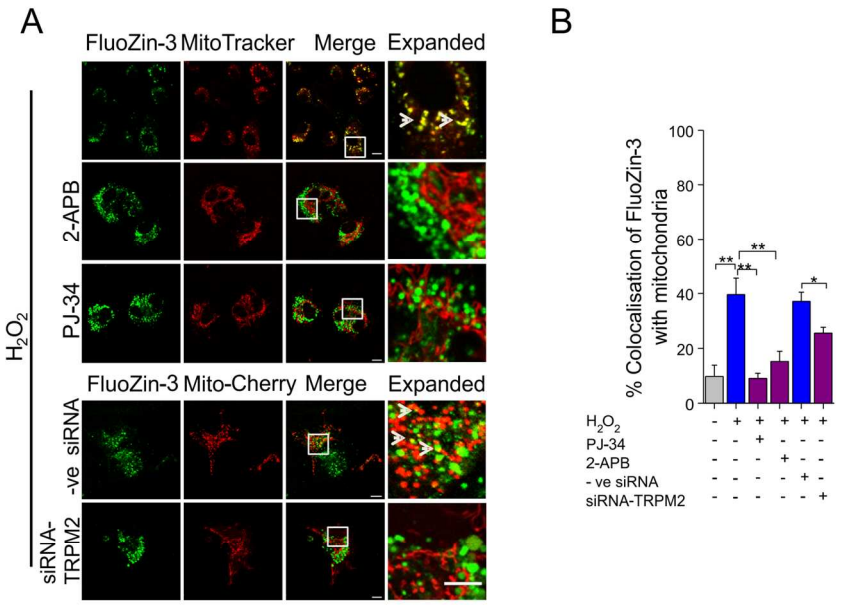

Fig. S9. H_2O_2-induced increase in mitochondrial Zn^{2+} is TRPM2 dependent. (**A**) Live cell fluorescent images of HUVECs following exposure to 1 mM H_2O_2 (4 hr, 37°C); cells were co-treated with PJ34 (10 μM) or 2-APB (150 μM) or pre-transfected with scrambled siRNA or TRPM2-siRNA. Confocal images show FluoZin-3 and mitochondrial staining and indicate presence of Zn^{2+} in mitochondria (yellow in merged images); scale bar, 10 μm. Boxed regions in the merged images are magnified in the far right panels, with arrows highlighting yellow puncta; scale bar, 5 μm. (**B**) Mean ± SEM of data from (A), expressed as percent co-localisation of Zn^{2+} with mitochondria. n=3 independent experiments. Minus H_2O_2, 105 cells; H_2O_2, 122 cells; PJ34 = 100 cells; 2-APB, 88 cells; scrambled siRNA, 127 cells; siRNA-TRPM2, 68 cells. Statistical significance was assessed by one-way ANOVA with Tukey's post-hoc test, *p <0.05, **P < 0.01.

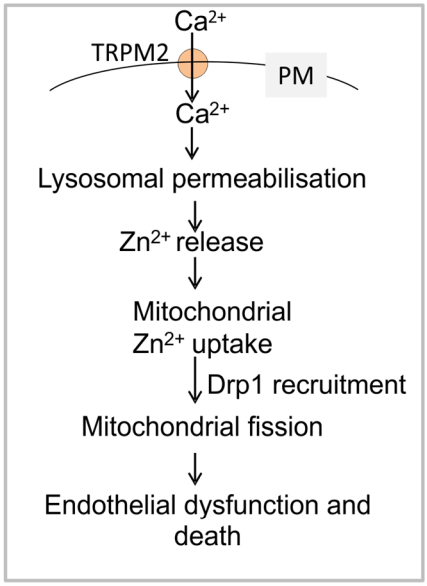

Fig. S10. Signaling cascade associated with oxidative stress-induced mitochondrial fragmentation. Schematic illustration of the signaling cascade determined from the data presented in the study. High glucose-induced oxidative stress leads to the activation of plasma membrane TRPM2 channels and Ca^{2+} influx. The resulting increase in intracellular Ca^{2+} triggers lysosomal permeabilisation and redistribution of lysosomal Zn^{2+} to mitochondria, where it promotes recruitment of cytoplasmic Drp-1 and thereby mitochondrial fragmentation.